J. Fluid Mech. (1995), *vol.* 296, *pp.* 73–126

Two-dimensional secondary instabilities in a strongly stratified shear layer

By CHANTAL STAQUET

Laboratoire de Physique (CNRS, URA 1325), Ecole Normale Supérieure de Lyon,
46 allée d'Italie, 69364 Lyon Cédex 07, France

(Received 31 January 1994 and in revised form 14 February 1995)

In a stably stratified shear layer, thin vorticity layers ('baroclinic layers') are produced by buoyancy effects and strain in between the Kelvin–Helmholtz vortices. A two-dimensional numerical study is conducted, in order to investigate the stability of these layers. Besides the secondary Kelvin–Helmholtz instability, expected but never observed previously in two-dimensional numerical simulations, a new instability is also found.

The influence of the Reynolds number (*Re*) upon the dynamics of the baroclinic layers is first studied. The layers reach an equilibrium state, whose features have been described theoretically by Corcos & Sherman (1976). An excellent agreement between those predictions and the results of the numerical simulations is obtained. The baroclinic layers are found to remain stable almost up to the time the equilibrium state is reached, though the local Richardson number can reach values as low as 0.05 at the stagnation point. On the basis of the work of Dritschel *et al.* (1991), we show that the stability of the layer at this location is controlled by the outer strain field induced by the large-scale Kelvin–Helmholtz vortices. Numerical values of the strain rate as small as 3 % of the maximum vorticity of the layer are shown to stabilize the stagnation point region.

When non-pairing flows are considered, we find that only for $Re \geqslant 2000$ does a secondary instability eventually amplify in the layer. (*Re* is based upon half the initial vorticity thickness and half the velocity difference at the horizontally oriented boundaries.) This secondary instability is not of the Kelvin–Helmholtz type. It develops in the neighbourhood of convectively unstable regions of the primary Kelvin–Helmholtz vortex, apparently once a strong jet has formed there, and moves along the baroclinic layer while amplifying. It next perturbs the layer around the stagnation point and a secondary instability, now of the Kelvin–Helmholtz type, is found to develop there.

We next examine the influence of a pairing upon the flow behaviour. We show that this event promotes the occurrence of a secondary Kelvin–Helmholtz instability, which occurs for $Re \geqslant 400$. Moreover, at high Reynolds number ($\geqslant 2000$), secondary Kelvin–Helmholtz instabilities develop successively in the baroclinic layer, at smaller and smaller scales, thereby transferring energy towards dissipative scales through a mechanism eventually leading to turbulence. Because the vorticity of such a two-dimensional stratified flow is no longer conserved following a fluid particle, an analogy with three-dimensional turbulence can be drawn.

---

1. Introduction

Stably stratified turbulent fluids exist in most natural systems, ranging from lakes to stars and are present in a number of industrial devices. The action of the buoyancy force compels the flow to organize into quasi-horizontal layers, as revealed for instance by *in situ* measurements in the ocean; the patchlike nature of stratified turbulence has motivated models for the oceanic mixing at small scales, based upon the vertical superposition of well-mixed layers separated by thin sheets of strong density and velocity gradients (see Gregg 1987 for a review). As well, in the atmosphere, it is in these sheets that clear air turbulence frequently occurs (e.g. Dutton & Panofski 1970). The organization of turbulent stably stratified flows into quasi-horizontal layers can also be observed in the wake experiments by Lin & Pao (1979), in the experiments with an oscillating grid by Browand, Guyomar & Yoon (1987) or in the numerical simulations of strongly stratified forced homogeneous turbulence by Herring & Métais (1989). Such horizontal layering may also be inferred from the ratio of vertical to horizontal lengthscales in the wind-tunnel experiment by Lienhardt & Van Atta (1990) or in the numerical calculations by Gerz & Schumann (1991), where a homogeneous mean shear is present. (See Hopfinger 1987 and Thorpe 1987 for reviews of stably stratified turbulence.) The spontaneous existence in stably stratified turbulence of quasi-horizontal layering and local velocity shear has motivated the present numerical study of a model flow consisting of the stably stratified shear layer. In this paper, we focus on the generation of two-dimensional secondary instabilities. Our computations will bring to the fore a mechanism for the onset of turbulence in a strongly stratified shear flow, consisting of the development, at high Reynolds numbers, of successive secondary instabilities in vorticity layers that form in the flow.

As quoted in Drazin & Reid (1981, p. 332), the inviscid theory gives a useful criterion for the overall stability of such a flow at large Reynolds number. The temporal stability of an inviscid stably stratified shear layer within the Boussinesq approximation is reviewed in that monograph. The growing instability, of the Kelvin–Helmholtz type, is symmetric at the interface and non-dispersive. A necessary condition for instability to grow from an infinitely small disturbance is that the Richardson number is smaller than 0.25 somewhere in the flow (Miles 1961; Howard 1961). The Richardson number is proportional to the ratio of the mean density gradient over the mean vorticity squared (and is often referred to as the gradient Richardson number). Its minimum value at $t = 0$ will be denoted J hereafter. This necessary condition has actually been shown numerically to be sufficient by Hazel (1972) for basic density and velocity profiles of hyperbolic tangent type, by solving the linear stability equation for an inviscid flow. Predictions of the linear theory have been examined experimentally by Thorpe (1971) and by Scotti & Corcos (1972) and numerically by Patnaik, Sherman & Corcos (1976) (viscosity being taken into account in the latter case). In many experimental studies however, the thickness of the initial velocity profile exceeds the thickness of the initial density profile by at least a factor two (e.g. Browand & Winant 1973; Yoshida 1977; Koop & Browand 1979; Lawrence, Browand & Redekopp 1991). In this case, and when $J \geqslant 0.07$, a dispersive instability, the Holmboe instability, dominates the earlier flow dynamics (the Kelvin–Helmholtz instability being prevalent for $J \leqslant 0.07$). We shall not consider this case in the present study.

As the development of the Kelvin–Helmholtz instability proceeds, a streamwise density gradient occurs in between the Kelvin–Helmholtz vortices, at the location where the 'braids' form in an unstratified shear layer. This streamwise density gradient (corresponding to the spanwise component of the baroclinic torque, in the Boussinesq approximation) feeds the braid with vorticity. It follows that vorticity can locally increase beyond its maximum initial value, even if the flow dynamics is two-dimensional. This property yields a fundamentally different behaviour of the two-dimensional stratified shear layer as opposed to its unstratified counterpart: thin tilted layers of strong vorticity are formed in between the (now weakened) Kelvin–Helmholtz vortices. Such baroclinic layers, as they will be referred to hereafter, can be clearly seen in the two-dimensional numerical simulations of Patnaik *et al.* (1976), Peltier, Hallé & Clark (1978), Davis & Peltier (1979) or Klaassen & Peltier (1985*a–c*, 1989, 1991). The question of whether a secondary Kelvin–Helmholtz instability can appear in these baroclinic layers has been raised in these articles (as well as in Corcos & Sherman 1976). In the review article by Thorpe (1987), this secondary instability is sketched as one of the mechanisms which could trigger turbulence in a stably stratified shear layer. For this reason, it is one of the mechanisms by which mixing is supposed to occur in the ocean (Woods 1969).

Other instabilities can develop in a stably stratified shear layer (see Klaassen & Peltier 1991). Some of these correspond to the instabilities that develop in shear layers with uniform density, the stable stratification having an overall stabilizing effect on them, even suppressing if strong; others are inherent to stable stratification. In the first class can be mentioned the two-dimensional subharmonic instability, leading to the pairing of Kelvin–Helmholtz vortices and, in three dimensions, a vortex stretching mechanism in the braid region, and an instability in the vortex core. The former mechanism leads to longitudinal streamwise or 'rib' vortices. A theoretical model of these rib vortices has been proposed by Lin & Corcos (1984); numerous experimental studies of these vortex structures have also been conducted (e.g. Bernal & Roshko 1986; Lasheras, Cho & Maxworthy 1986; Nygaard & Glezer 1991), as well as numerical investigations (Metcalfe *et al.* 1987; Rogers & Moser 1992; Comte, Lesieur & Lamballais 1992). Concerning the instability in the vortex core, a review of its theoretical discovery can be found in Bayly, Orszag & Herbert (1988) and numerical evidence is provided in Knio & Ghoniem (1992). The second class of instabilities, inherent to stable stratification, essentially contains a three-dimensional convective instability due to a local inversion of the vertical density gradient; this instability has been conjectured by Davis & Peltier (1979) and observed experimentally by Thorpe (1985, 1987), Lawrence *et al.* (1991) and, most clearly, by Schowalter, Van Atta & Lasheras (1994). Numerical evidence of the convective instability has also been provided by Caulfield & Peltier (1994). The two-dimensional secondary Kelvin–Helmholtz instability mentioned above belongs evidently to this second class, in the sense that the basic flow upon which it develops, the baroclinic layer, does not exist in an unstratified shear flow.

To our knowledge, evidence for the occurrence of this secondary instability has only been reported in observations of geophysical flows (e.g. in the atmosphere, Gossard, Richter & Atlas 1970; in the ocean, Haury, Briscoe & Orr 1979), in very few laboratory experiments (Delisi 1973 and private communication 1994; Altman 1988; Atsavapranee 1995) and in only one three-dimensional numerical simulation (Staquet 1991).

Hints concerning the occurrence of this secondary instability had previously been obtained by several authors. Thorpe (1968) observed secondary small-scale waves and spiral rolls in the baroclinic layer. The same observation was reported by Woods (1969) in the oceanic thermocline. In the highest Reynolds number case ($Re = 900$) of the numerical simulations performed by Klaassen & Peltier (1985*a*) some irregularities are reported in the density field of the baroclinic layer; unfortunately, the associated vorticity field is not shown. The Reynolds number is based upon half the initial vorticity thickness and half the initial velocity difference at the horizontally oriented boundaries. From a theoretical point of view, Corcos & Sherman (1976) derived an analytical model for the dynamics of a baroclinic layer. This model yields, in particular, an analytical expression for the Richardson number of the baroclinic layer, from which Corcos & Sherman conclude that only for a high enough value of the initial Reynolds number may the layer become unstable (in the sense of the Miles–Howard theorem). In Klaassen & Peltier (1989), the stability to two-dimensional perturbations of a basic flow consisting of non-pairing quasi-steady Kelvin–Helmholtz vortices with $J = 0.07$ is examined. An eigenmode corresponding to a wavevector of zero component both in the streamwise and spanwise directions has been isolated at the stagnation point of the baroclinic layer. Those authors suggested that this mode may correspond to the two-dimensional secondary instability in question here and related it to Thorpe's (1968) and Woods' (1969) observations of small-scale waves.

In the present paper, the occurrence of a secondary instability in a baroclinic layer is clearly shown using two-dimensional direct numerical simulations of the Navier–Stokes equations in the Boussinesq approximation. We shall only consider strongly stratified shear layers, with $J = 0.167$. The search for secondary instabilities in the baroclinic layers will lead us to vary the initial Reynolds number of the flow and values up to 2600 will be considered.

As noted above, two-dimensional numerical simulations of a stably stratified shear layer in a vertical plane have already been performed, starting with Patnaik *et al.* (1976). In this latter paper, the development of one Kelvin–Helmholtz vortex for various initial conditions and different values of the initial Reynolds number (up to 200) and minimum Richardson number of the flow is examined. The influence of these parameters upon the braid history, the state of maximum amplitude of the Kelvin–Helmholtz wave and its subsequent evolution are studied in detail. Higher-resolution calculations (128×129) have been performed by Klaassen & Peltier. In Klaassen & Peltier (1985*a*) the influence of the Reynolds number (up to 900, with $J = 0.07$) upon the flow evolution is studied, while in Klaassen & Peltier (1985*b*) the effect of the Prandtl number upon that evolution is examined (with $J = 0.07$ and $Re = 300$). Numerical simulations of vortex pairings of two and three vortices in a moderately stratified fluid are presented in Klaassen & Peltier (1989). The influence of the initial condition upon vortex pairings is examined, as well as the late flow behaviour. These calculations have been also used to test the linear stability of a quasi-steady Kelvin–Helmholtz vortex against two-dimensional perturbations (Klaassen & Peltier 1989). In Klaassen & Peltier (1991), the linear stability of this basic state is tested against three-dimensional perturbations, for different values of parameter J (ranging between 0 and 0.16), thereby complementing an earlier study (Klaassen & Peltier 1985*c*).

The present paper is organized as follows. The numerical model is presented in §2. In order to understand why a secondary Kelvin–Helmholtz instability was not found in previous two-dimensional numerical calculations, the structure and dynamics of the baroclinic layer in the neighbourhood of its stagnation point are studied in detail, as a function of the Reynolds number. For this purpose, the analytical model proposed by Corcos & Sherman (1976) is used and carefully tested against our numerical results (§3). The stabilizing influence of the outer strain field acting upon the baroclinic layer in the neighbourhood of its stagnation point is next discussed, on the basis of the work by Dritschel *et al.* (1991). The late development of secondary instabilities is described in §4, together with the influence of the pairing process on the growth of these instabilities. The analogy of the flow dynamics with three-dimensional turbulence is also investigated. In §5, the results are summarized and conclusions are drawn.

2. Mathematical model and numerical method

2.1. *Mathematical model*

Let (x, y, z) be a Cartesian coordinate system where x is in the streamwise (mean flow) direction, y in the spanwise direction and z points upwards. The unit vectors along these three directions are denoted $\boldsymbol{i}_x$, $\boldsymbol{i}_y$ and $\boldsymbol{i}_z$ respectively. We study a temporal shear layer, that is a flow which is statistically uniform in the horizontal plane and develops in time. This problem is more tractable numerically than the spatial shear layer (which would correspond to most experimental studies). A spatial shear layer is statistically steady in time but develops along the streamwise direction; appropriate inflow–outflow boundary conditions are thus required along that direction. A Galilean transformation can be used to relate the spatial problem to the temporal one: $x = \bar{U}t$, where $\bar{U}$ is the mean velocity in the spatial problem. This transformation is strictly valid when the velocity difference between the two streams is small compared to the mean velocity. Actually, as shown by previous numerical studies of a temporal shear layer (e.g. Metcalfe *et al.* 1987; Rogers & Moser 1992), the validity of the transformation extends beyond the limits imposed by this condition.

We assume that the fluid motion is described by the two-dimensional Navier–Stokes equations in the Boussinesq approximation:

$$\frac{\partial \omega}{\partial t} + \mathcal{J}(\omega, \psi) = \frac{g}{\rho_0}\frac{\partial \rho}{\partial x} + \nu \nabla^2 \omega, \quad \frac{\partial \rho}{\partial t} + \mathcal{J}(\rho, \psi) = \kappa \nabla^2 \rho. \tag{2.1}$$

ψ is a stream function related to the velocity field by

$$u = -\partial\psi/\partial z, \quad w = \partial\psi/\partial x. \tag{2.2}$$

In this two-dimensional situation, the vorticity field has only one non-zero component, along the spanwise direction: $\omega = (\nabla \times \boldsymbol{u})\cdot \boldsymbol{i}_y$, which is related to the stream function by $\omega = -\Delta\psi$. As well, the baroclinic torque, which only involves density gradients in the Boussinesq approximation (being equal to $-g/\rho_0(\nabla\rho \times \boldsymbol{i}_z)$), is simply proportional to the streamwise gradient of the density in two dimensions. $\mathcal{J}$ is the Jacobian function ($\mathcal{J} \equiv (\partial/\partial x)(\partial/\partial z) - (\partial/\partial z)(\partial/\partial x)$); $-g\boldsymbol{i}_z$ is the acceleration due to gravity; ν denotes the kinematic viscosity and κ is the diffusion coefficient for density changes. ρ is the total density field.

We decompose ρ as

$$\rho(x, z, t) = \rho_0 + \bar{\rho}(z, t) + \rho'(x, z, t), \tag{2.3}$$

where ρ_0 is a constant density reference, $\bar{\rho}(z, t)$ is the mean density and ρ' is the deviation from the mean. The initial condition is defined in terms of the density and velocity fields, the stream function being next computed from (2.2). As in Patnaik *et al.* (1976), the initial mean velocity and mean density profiles are the similarity solutions of the Boussinesq equations that would result from the action of molecular effects upon a discontinuity of horizontal velocity and density at $z = 0$:

$$\bar{U}_i(z) = U \operatorname{erf}\left(\frac{\pi^{1/2}}{2}\frac{z}{\delta_i}\right), \tag{2.4a}$$

$$\bar{\rho}_i(z) = -\frac{\Delta\rho}{2} \operatorname{erf}\left(\frac{\pi^{1/2}}{2}\frac{z}{\delta_i/Pr^{1/2}}\right), \tag{2.4b}$$

where δ_i is half the initial vorticity thickness of the shear layer. $Pr = \nu/\kappa$ is the Prandtl number; it has a value of 0.7 for all the calculations presented in this paper, which is the value for air at standard temperature and pressure. The ratio of the thickness of the density profile to that of the velocity profile is equal to $Pr^{-1/2}$, and is therefore close to 1. These two profiles are plotted in figure 1.

No density perturbation is superposed initially upon the mean density profile. By contrast, two-dimensional perturbations are superimposed upon the mean velocity field at $t = 0$, in order to promote the development of the Kelvin–Helmholtz instability and pairing when two Kelvin–Helmholtz vortices develop in the numerical domain. These two-dimensional perturbations are respectively solutions of the Rayleigh equation for the fundamental wavenumber α and for its first subharmonic $\alpha/2$. α is the most amplified wavenumber predicted by inviscid linear stability theory for a velocity profile of error-function type and is equal to $0.4391/\delta_i$. The amplitude of the perturbation velocity for the fundamental mode is equal to $\epsilon_{2D} = 0.11U$ for all calculations. As for the subharmonic mode, calculations with two different initial amplitudes will be performed, equal to either $\epsilon_{2D}/2.5$ or $\epsilon_{2D}/10$. According to the analysis of Klaassen & Peltier (1989, p. 387), the former amplitude for the subharmonic mode corresponds to a forced shear layer for pairing, the ratio between the kinetic energy of the fundamental and subharmonic modes exceeding a threshold value that these authors estimated to be about 10. The latter amplitude yields a ratio of 77 between the kinetic energy of these two Fourier components and, according to the criteria established numerically by Klaassen & Peltier, would correspond to an unforced situation. It should be noticed that, in the present paper, pairing is observed to occur for both amplitudes, even for a value of the Reynolds number as low as 400. By contrast, Koop & Browand (1979) reported that, on an average, this event did not occur for the same value of J in their $Re \approx 300$ experimental study. The initial density and velocity profiles in the experiment were, however, different from the present case and, for our value of J, led to a process of interfacial breaking waves through Holmboe instability.

For boundary conditions, we assume that the flow is periodic in the streamwise direction, and at the horizontally oriented boundaries take free slip conditions on the velocity. These boundary conditions are consistent with the temporal shear layer problem. However, the free-slip boundary conditions require that $\rho - \rho_0 = 0$ at the horizontally oriented boundaries, which is incompatible with the choice of the initial density profile. Such a problem can be solved by writing the total density field as

$$\rho(x, z, t) = \rho_0 + \tilde{\rho}(x, z, t) + \rho_{lin}(z) \tag{2.5}$$

and choosing $\rho_{lin}(z)$ so that $\tilde{\rho}(x, z, t) = 0$ at the z-boundaries at any time; this condition implies that $\rho_{lin}(z)$ has to be defined by

$$\rho_{lin}(z) = -\Delta\rho\, z/L_z, \tag{2.6}$$

where L_z is the distance between the horizontally oriented boundaries. Equations (2.1) have thus been rewritten in terms of density variable $\tilde{\rho}$, instead of ρ, before being solved numerically. Note that, by (2.3) and (2.5), $\tilde{\rho}(x, z, t)$ is equal to $\bar{\rho}(z, t) + \rho'(x, z, t) - \rho_{lin}(z)$, from which it follows that $\tilde{\rho}$ and $\bar{\rho}$ are related by

$$\bar{\tilde{\rho}}(z, t) = \bar{\rho}(z, t) - \rho_{lin}(z). \tag{2.7}$$

This relation is used in particular to initialize $\tilde{\rho}$. To permit physical interpretation however, all results will be expressed in terms of the density variable $\rho - \rho_0$ throughout the paper.

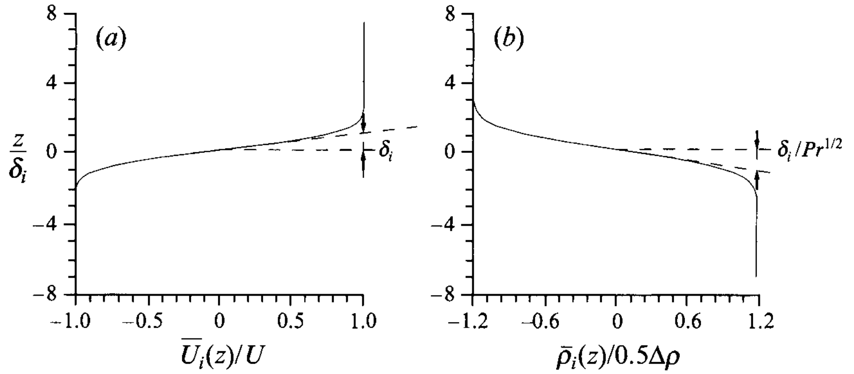

FIGURE 1. Initial mean velocity (*a*) and mean density (*b*) profiles. Half the thickness of each profile is plotted ($2\delta_i$ is the vorticity thickness at $t = 0$).

Run	Comments	(N_x, N_z)	Resolution	Re	$\Delta\rho_L$	t_{NC}	t_{KH}
1	$J = 0$	(2,2)	(512,513)	200	—	x	x
2		(1,1)	(128,129)	140	1.62	x	x
3		(1,1)	(256,257)	400	1.70	x	x
4		(1,1)	(512,513)	1000	1.77	*	x
5		(1,1)	(768,769)	1500	1.77	44.5	x
6		(1,1)	(1024,1025)	2000	1.76	44	72
7		(1,1)	(1536,1537)	2600	1.78	43.5	67
8	Same as run 4 except that $E(\alpha, t = 0)$ has been divided by 10^4	(1,1)	(256,257)	1000	—	—	—
9	Pairing with $E(\frac{1}{2}\alpha, t = 0) = E(\alpha, t = 0)/4.8$	(2,1)	(512,257)	400	—	x	91
10		(2,1)	(768,385)	1000	—	*	81
11		(2,1)	(1024,513)	1500	—	44	64
12		(2,1)	(1536,769)	2000	—	43	62
13	Pairing with $E(\frac{1}{2}\alpha, t = 0) = E(\alpha, t = 0)/77$	(2,1)	(512,257)	400	—	x	97
14		(2,1)	(1536,769)	2000	—	43	65
15	White noise perturbation	(4,1)	(1024,257)	1000	—	—	114

x: No secondary instability.
*: Only the perturbation at the origin of the instability is visible from $t \approx 44$, before decaying.
—: Not available or not computed.

TABLE 1. Description of the calculations. N_x and N_z are the size of the computational domain along the streamwise and vertical directions respectively, non-dimensionalized by the fundamental wavelength. N_x thus corresponds to the number of primary Kelvin–Helmholtz vortices that are able to develop in the flow. Re: initial Reynolds numbers (defined in §2.1); $\Delta\rho_L$: (positive) density difference across the baroclinic layer at $t = 52$ (defined in §3.3.2); t_{NC} and t_{KH}: (approximate) time at which the near-core and Kelvin–Helmholtz secondary instabilities onset (onset is defined from constant-vorticity maps, when the perturbation initiating the instability becomes visible); $E(\alpha, t = 0)$, $E(\frac{1}{2}\alpha, t = 0)$: initial kinetic energy in the fundamental and subharmonic wavenumbers respectively; $E(\alpha, t = 0) = 1.14 \times 10^{-4}$, except for runs 8 and 15; $J = 0.167$ and $Pr = 0.7$ for all calculations, except for run 1 which is unstratified.

Equations (2.1) have been solved numerically in dimensionless form. The length and velocity scales are δ_i and U respectively and time is made dimensionless using the advective time scale δ_i/U. The density is scaled by $Pr^{1/2}\Delta\rho/2$. With this scaling, the dimensionless parameters which come into play in the equations are: Re, the Reynolds number, initially equal to $U\delta_i/\nu$; the minimum Richardson number, whose expression at $t = 0$ is

$$J = \min_z -\frac{g}{\rho_0}\left[\frac{\mathrm{d}\bar{\rho}_i}{\mathrm{d}z} \Big/ \left(\frac{\mathrm{d}\bar{U}_i}{\mathrm{d}z}\right)^2\right] = g\frac{\Delta\rho}{\rho_0}\frac{Pr^{1/2}}{2}\frac{\delta_i}{U^2}, \tag{2.8}$$

and the Prandtl number. As already noted in the Introduction, J has the constant value of 0.167 throughout the paper while Re varies between 140 and 2600. The Brunt–Väisälä period is defined by $2\pi/J^{1/2}$ and is thus equal to the largest period of the internal waves that propagate in the flow. It has a value of $15.4\delta_i/U$ in the present case.

2.2. *Numerical method*

Equations (2.1), written in dimensionless form and in terms of density variable $\tilde{\rho}$, have been solved using a pseudo-spectral method (e.g. Canuto *et al.* 1988): the spatial derivatives are computed in Fourier space while the nonlinear terms are computed in physical space. Along the vertical direction where free slip boundary conditions are imposed, the use of Fourier transforms is made possible by symmetrizing the velocity components and the density field about the z-boundary (Orszag 1971, Appendix II). On the doubled domain, u is expanded in a cosine series in z and w and $\tilde{\rho}$ in a sine series in z, which enforces the boundary conditions.

The computation of the nonlinear terms in physical space generates aliasing errors, which are eliminated by a standard truncation method (Canuto *et al.*, p. 84). The time advancement scheme is a third-order Adams–Bashforth scheme. The viscous terms are computed explicitly, because the Reynolds number of our calculations is large enough for the stability condition to be imposed by the advective time scale and not by the diffusive time scale (Canuto *et al.*, p. 204). The time step $\mathrm{d}t$ is such that $M\,\mathrm{d}t = 3.64$ where M is the number of grid points per wavelength $2\pi/\alpha$.

2.3. *Numerical accuracy of the calculations*

In the calculations presented in this paper, J and Pr are kept constant while Re is varied. For a given Reynolds number, we wish to determine which resolution ensures that the computation is reliable. For this purpose, we first check that the equation driving the evolution of the total enstrophy Z

$$Z = \langle(\nabla \times \boldsymbol{u})^2\rangle \tag{2.9}$$

is satisfied within at least 1 %. $\langle\ \rangle$ denotes a spatial average over the numerical domain. The equation for Z is

$$\frac{\mathrm{d}Z}{\mathrm{d}t} = J\left\langle \omega\frac{\partial\rho}{\partial x}\right\rangle - \frac{1}{Re}\left\langle\left(\frac{\partial\omega}{\partial x}\right)^2 + \left(\frac{\partial\omega}{\partial z}\right)^2\right\rangle. \tag{2.10}$$

Though this criterion involves second derivatives of the velocity field, it is a global one. Thus, even when it is satisfied, a local quantity of interest for the present study (defined by (3.10)), which also involves second derivatives of the velocity field, appears to temporarily exhibit spurious fluctuations. When this occurs, we increase the resolution by 50 % in each direction. As a result, these fluctuations are smoothed out while all other quantities of interest for the present study are nearly unchanged (for instance, the maximum vorticity of the flow over the numerical domain varies by at most 0.5 % as time evolves, when this resolution is increased). The resolution of the calculations presented in this paper, indicated in table 1, has been determined according to this local criterion.

3. Influence of the Reynolds number on the dynamics of a two-dimensional baroclinic layer

3.1. *Evolution of the unstratified shear layer*

Numerous two-dimensional numerical studies of an unstratified shear layer have already been published and are reviewed in Corcos & Sherman (1984) and Ho & Huerre (1984). We briefly recall the mechanisms that drive the evolution of a shear layer with uniform density, for comparison with the stably stratified case. An unstratified calculation is thus presented, in which the size of the computational domain is chosen so that two Kelvin–Helmholtz vortices can develop and merge: the horizontal (streamwise) and vertical lengths are equal to $4\pi/\alpha$. The velocity amplitude of the subharmonic perturbation is analogous to that of the forced shear layer for pairing (see §2.1). The initial Reynolds number is set to 200. The other parameters of this calculation, referred to as run 1, are written in table 1.

The mechanisms that lead to the formation of Kelvin–Helmholtz vortices are now well known and have been analysed by Batchelor (1967, p. 515) and Corcos & Sherman (1976). These are illustrated via constant contours of the vorticity at successive times (figure 2). The initial vorticity, whose streamwise distribution is slightly modulated by a small perturbation (figure 2*a*), progressively accumulates in regions which are periodically spaced in that direction (figures 2*b*, *c*). These regions will become the cores of the Kelvin–Helmholtz vortices. They induce upon the fluid located between them a strain field that advects vorticity to the cores. The regions of strong strain are usually called the braids. As noted by Corcos & Sherman (1976), the rate of strain is essentially proportional to the circulation around the core and the efficiency of the mechanism of vorticity accumulation thus increases with increasing core circulation. Note that during this process of instability growth, the growing quantity is not the vorticity of the cores but the circulation around those cores. Indeed, in the present case where the density is uniform, the vorticity is a Lagrangian invariant of the inviscid flow and, therefore, its maximum value can only decrease from $t = 0$ if the fluid is viscous (e.g. Kraichnan & Montgomery 1980).

As shown by Kelly (1967) and Klaassen & Peltier (1989), the vortex cores are most unstable to perturbation of wavenumber equal to $\alpha/2$. The growth of this subharmonic perturbation leads to the pairing of the two vortices (figure 2*d*) and the resulting vortex has roughly twice the size of the pairing vortices (figure 2*e*). That vortex then relaxes towards a stationary state, except for a slight diffusion and a weak oscillatory motion around the horizontal axis, referred to as the nutation phenomenon (Ho & Huerre 1984 and references therein, Klaassen & Peltier 1985*a*).

3.2. *Formation of baroclinic layers in a strongly stratified shear layer*

In this section, we first show how a baroclinic layer forms in a strongly stratified shear flow. For this purpose, a calculation where two Kelvin–Helmholtz vortices develop is presented. This allows us also to show that pairing occurs very slowly and that, therefore, the earlier evolution of the shear layer can be studied by considering the development of one Kelvin–Helmholtz vortex only. This observation will be taken into account in the next section, when comparing with the model of Corcos & Sherman.

The evolution of a strongly stratified shear layer is illustrated in figure 3 via contours of constant vorticity and density. The subharmonic mode has the same initial amplitude as in the unstratified calculation described above. However, since the amplitude of vertical motions is severely reduced by the strong stratification, a domain size equal to only $2\pi/\alpha$ along the vertical direction needs to be used. As well, though

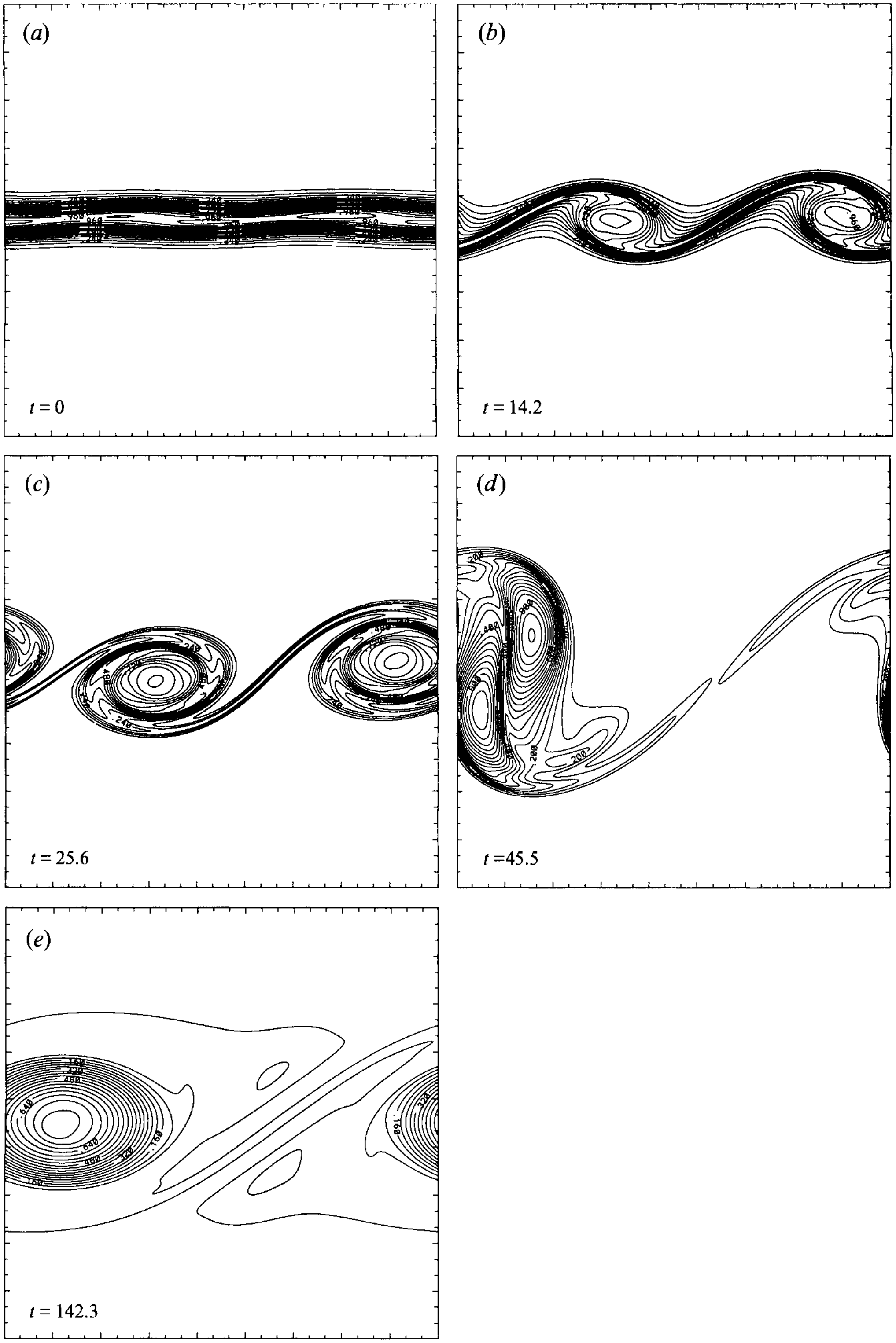

FIGURE 2. For caption see facing page.

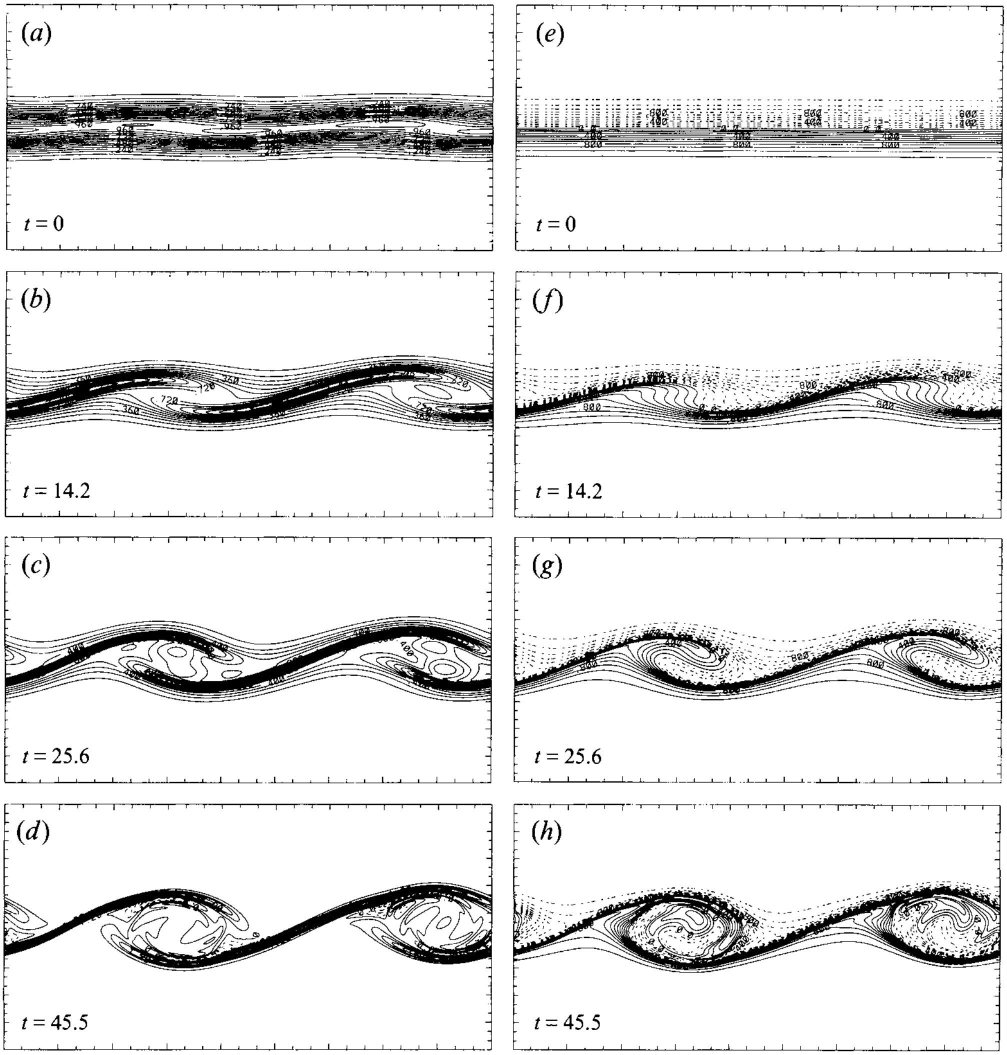

FIGURE 3. Run 10 ($Re = 1000$). (*a–d*) Contours of constant vorticity. (*a*) $\Omega_{max} = 1.02$, $d = 0.06$; (*b*) $\Omega_{max} = 1.44$, $d = 0.09$; (*c*) $\Omega_{max} = 2.7$, $d = 0.1$; (*d*) $\Omega_{max} = 3.6$, $d = 0.3$. Ω_{max} is the maximum vorticity (reached at the stagnation point of the baroclinic layers) and d is the distance between contour levels. Dashed-line contours represent negative values. (*e–h*) Contours of constant density corresponding to (*a–d*). $d = 0.1$.

the mesh size is nearly the same in both calculations, the stabilizing effect of the stratification upon the overall flow dynamics permits us to increase the initial Reynolds number. According to the criterion described in §2.3, a value of 1000 (instead of 200 in the unstratified case) can thus be employed. This calculation is referred to as run 10 in table 1.

Figure 3 shows that the growth of the instability mainly results in the formation of two stretched layers of vorticity (figure 3*b–d*). The same layers are also seen as regions of strong streamwise density gradients (figure 3*f–h*); these regions will thus be referred

FIGURE 2. Contours of constant vorticity for a two-dimensional shear layer with uniform density (run 1 in table 1). The distance between contour levels is equal to (*a*) 0.06; (*b*) 0.06; (*c*) 0.06; (*d*) 0.05; (*e*) 0.04.

to as 'companion density layers' hereafter. The vorticity and companion density layers together form a baroclinic layer. In order to illustrate the essential role of the companion density layer in vorticity changes of the flow, through the baroclinic torque, we have represented in figure 4 the temporal evolution of the vorticity (figure 4*a*) and of the spanwise component of the baroclinic torque (figure 4*b*) at four different locations in the flow: at the stagnation point of the two baroclinic layers and at the centre of the Kelvin–Helmholtz vortices.

Figure 4(*b*) shows that, from $t \geqslant 3$, the streamwise gradient of the density continuously reinforces the vorticity in the baroclinic layers. By contrast, it weakens the vorticity at the centre of the vortex cores, except for short periods of time. From a global point of view, Corcas & Sherman (1976) pointed out that the baroclinic destruction in the core may be viewed as automatic compensation for baroclinic generation in the braids, since the total vorticity per wavelength remains constant. The baroclinic effects thus modify the development of the flow in two ways: (i) they weaken the vorticity accumulation process in the core (i.e. the growth of the circulation of the vortex core is reduced) and therefore prevent the instability from rapidly amplifying; (ii) baroclinic effects continuously feed the baroclinic layers with vorticity and thus make up for the advective loss. Figure 4(*a*) actually shows that the vorticity in these layers continuously increases up to $t \approx 50$; thus, at least up to this time, the rate at which vorticity is baroclinically produced in the layers is higher than that at which it is removed by advection towards the cores. (These two main features of the dynamics of the baroclinic layers are formalized in the model of Corcos & Sherman 1976 and will be examined in more detail in §3.3.) More precisely, the baroclinic production of vorticity is higher in the left-hand layer than in the right-hand one: the reason is that the left-hand layer is somewhat thinner than the right-hand one, for the same density difference (see figure 3*h*); the streamwise density gradient is thus higher there. The fact that the vorticity nevertheless increases at almost the same rate at the stagnation point of both layers suggests that the vorticity is removed at a greater rate in the left-hand layer than in the right-hand one. As justified in §4.5, this may be attributable to the fact that the Kelvin–Helmholtz vortices are closer to the left-hand stagnation point than to the right-hand one, very likely because the subharmonic instability has started to grow (see figure 5 below).

Note that, during the same time, two Kelvin–Helmholtz vortices would have already formed in the flow if the shear layer were unstratified, with braids almost depleted of vorticity (figure 2*c*), and that pairing would already be occurring (figure 2*d*). The lower value of the Reynolds number in this unstratified run does not invalidate our comparison because a higher Reynolds number would increase the growth rate of the fundamental and subharmonic perturbations and thus emphasize the difference in behaviour that is already observed.

The temporary growth of the vorticity in the cores displayed in figure 4(*a*) partly results from convective activity: potential energy is converted into kinetic energy when the heavy fluid that has been lifted as the initial vorticity layer rolls up is entrained towards the bottom of the vortex. The fluid is accelerated during this event and the local vorticity increases. Also, as the heavy fluid is entrained downward, the sign of the streamwise density gradient becomes positive again (see figure 3*g*), which contributes to the vorticity growth as well (figure 4*b*). The existence of convective motions can be seen easily by noting that the vorticity in the vortex core increases periodically, with a period ≈ 20 (figure 4*a*). This is of the same order as the period of rotation of a fluid particle inside the vortex, of diameter $\approx \pi/\alpha$, at a speed of order 1. This can be also clearly seen in figure 3(*g*, *h*): the heavy (and light) fluid particles have accomplished one

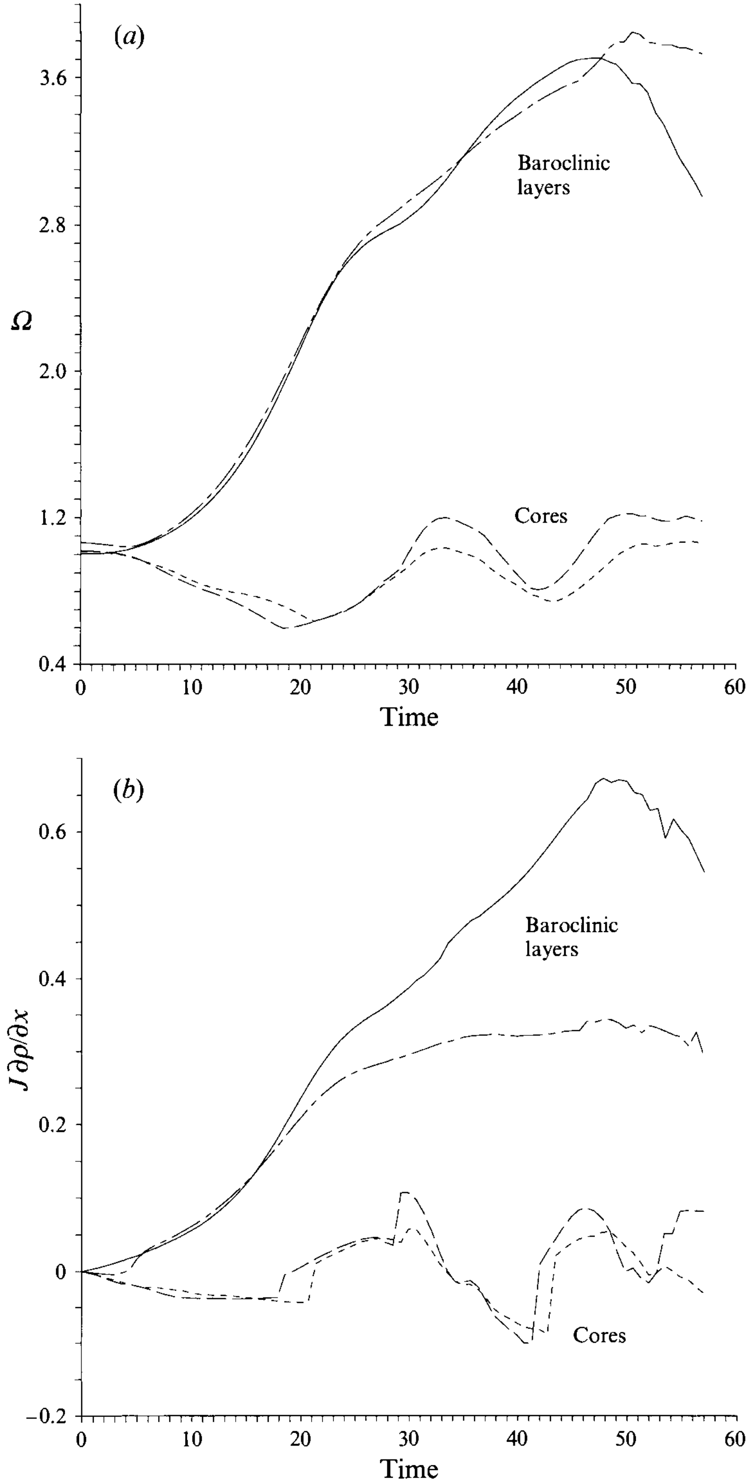

FIGURE 4. Run 10 ($Re = 1000$). (*a*) Evolution of the spanwise vorticity Ω at the stagnation point of the left-hand baroclinic layer (——), right-hand baroclinic layer (— — — —), at the centre of the left-hand vortex (— — — —) and right-hand vortex (– – – –). (*b*) Evolution of the spanwise component of the baroclinic torque $J\partial\rho/\partial x$ at these four locations.

full turn inside the vortex core during the (dimensionless) time, equal to about 20, separating these two figures. Convective activity is however too weak to make up for the overall opposing effect of the baroclinic torque in the instability growth. Such a result is in agreement with Klaassen & Peltier's (1985*a*) numerical study which shows that transfers from potential to wave kinetic energy play a secondary role in the wave development.

We have computed the height reached by the Kelvin–Helmholtz vortex once the fundamental perturbation has saturated (figure 3*d*) and compared it to a theoretical prediction of Corcos & Sherman (1976) and to the experimental measurement of Thorpe (1973). In Corcos & Sherman (1976), a second theoretical model is proposed, in addition to the one mentioned above for the dynamics of a baroclinic layer, which predicts the temporal evolution of the height of the Kelvin–Helmholtz vortex as a function of J. The Kelvin–Helmholtz vortex is modelled as a Stuart vortex (Stuart 1967) because of the close correspondence between the properties of the two velocity fields near the stagnation point. For the present simulations, the height of the Kelvin–Helmholtz vortex is defined by the distance along the vertical line joining the centre of this vortex to the centre of the baroclinic layer that surrounds it. According to the model of Corcos & Sherman, this height relative to the most amplified wavelength, H say, should reach an asymptotic value as time evolves equal to ≈ 0.145. It can be shown from figure 3(*d*) (and most clearly, from figure 7*d* below) that this expression accurately predicts the height found numerically, apart from a slight underestimation (by about 3 %). This underestimation was also predicted by Corcos & Sherman and attributed to the use of the Stuart vortex as model flow. In Thorpe (1973), laboratory experiments of a temporally growing stably stratified shear layer are presented. Figure 3 of Thorpe's paper displays twice the thickness H as a function of J (denoted R_I in that paper). We found a good agreement with Thorpe's measurement, for $R_I \approx 0.14$: indeed, it is clear from flow visualizations of the experiments (see figure 2 of Thorpe's paper) that our $J = 0.167$ calculations correspond to $R_I \approx 0.14$ experiments (the Reynolds numbers being of the same order).

Finally, note that, in the remainder of the present paper, the denomination 'model of Corcos and Sherman' will refer to the model for the baroclinic layer proposed by these authors in their 1976 article.

3.2.1. *Influence of the subharmonic mode upon the flow development*

Figures 3 and 4 show that two similar Kelvin–Helmholtz vortices and baroclinic layers develop in the flow up to $t \approx 55$, though a subharmonic perturbation with strong amplitude has been added at $t = 0$. The weak influence of this perturbation upon the behaviour of the flow up to this time can be estimated quantitatively from figure 5. The kinetic energy in the fundamental and subharmonic modes is plotted versus time in this figure, and compared with the kinetic energy in the fundamental mode when only one Kelvin–Helmholtz vortex develops in the flow (run 4 in table 1). Figure 5 shows that the subharmonic mode starts growing (after a transient initial growth) when the fundamental mode has saturated, an effect already noted in previous numerical simulations of shear layers, both unstratified (e.g. Corcos & Sherman 1984) and stratified (e.g. Klaassen & Peltier 1989). This final growth is however very slow in the present case of a strong stratification and only at $t \approx 54$ does the kinetic energy of the subharmonic mode become as high as that of the fundamental mode. As shown by figure 3(*d*), this is mainly manifested as a slight displacement of the right-hand vortex to the right toward the left-hand vortex (boundary conditions being periodic along the streamwise direction). As a result, the kinetic energy in the fundamental mode of the

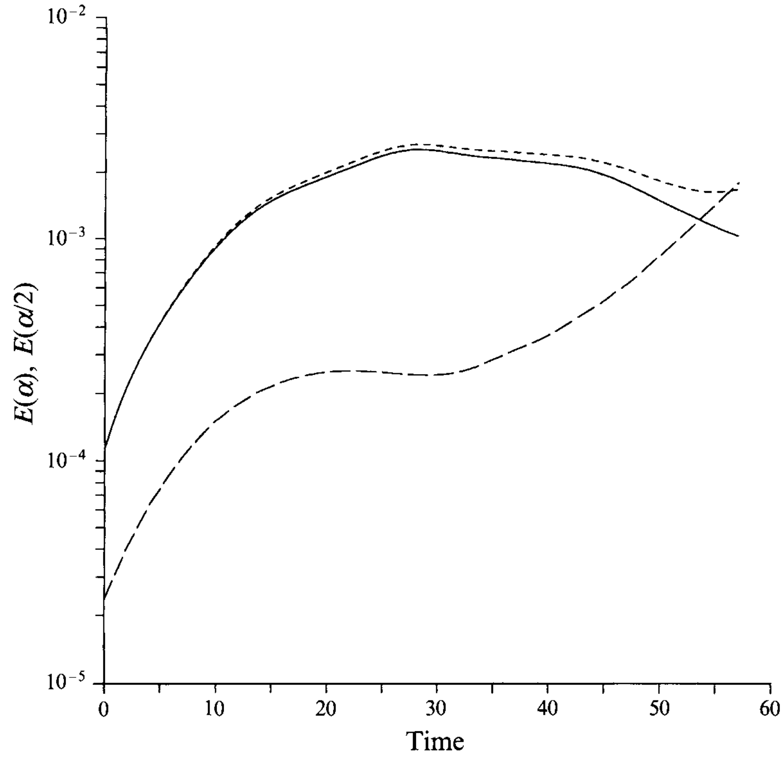

FIGURE 5. Influence of a subharmonic perturbation on the growth of the fundamental mode ($Re = 1000$): – – – –, kinetic energy in the fundamental mode $E(\alpha)$ when pairing is prohibited (run 4); ——, kinetic energy in the fundamental mode when a subharmonic perturbation exists (run 10); — — —, kinetic energy in the subharmonic mode $E(\alpha/2)$ for run 10.

one and two Kelvin–Helmholtz vortex flows exhibits similar behaviour up to $t \approx 54$. This suggests that the flow dynamics up to this time may be studied by considering the development of one Kelvin–Helmholtz vortex only.

3.2.2. *Influence of the initial amplitude of the perturbation upon the development of the flow*

Figure 5 shows that the growth rate of the fundamental mode does not attain a regime with a constant value at the beginning of the calculation. One reason may be that the initial amplitude of the perturbation is too high to lead to a linear regime. If this were true, it would be necessary to verify that the subsequent fully nonlinear development of the flow does not depend upon this initial amplitude. This question has been addressed qualitatively by Klaassen & Peltier (1985*a*, 1989) for the case of a weakly stratified shear layer.

In order to ensure that the earlier regime of the flow is linear, we have decreased the initial amplitude of the perturbation velocity ϵ_{2D} by a factor 100 (run 8 in table 1; to gain computation time, a shear layer with only one Kelvin–Helmholtz vortex developing is simulated). The kinetic energy in the fundamental mode $E(\alpha)$ corresponding to this calculation is plotted versus time in figure 6(*a*) (full line). In order to examine the influence of nonlinear interactions upon this growth, the same calculation has been carried out again, without nonlinear terms. The kinetic energy in the fundamental mode corresponding to this calculation (short-dash line) clearly shows that nonlinear effects start to influence the flow dynamics when $E(\alpha)$ exceeds a value

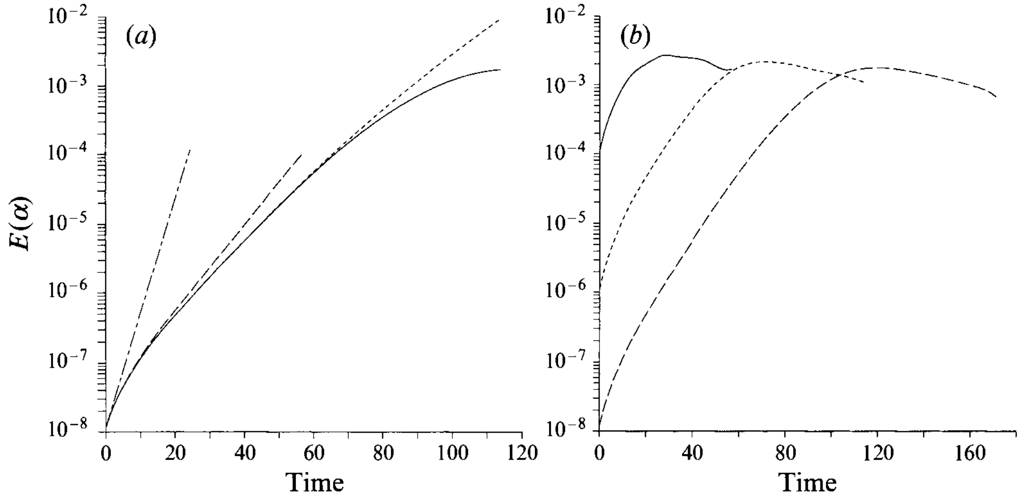

FIGURE 6. Temporal evolution of the kinetic energy of the fundamental mode $E(\alpha)$, for $Re = 1000$. (*a*) Influence of viscosity and nonlinear interactions upon this evolution: ——, the fully nonlinear viscous Boussinesq equations have been solved (run 8); ----, same calculation, without nonlinear effects; — — —, same calculation, without viscous effects (identical behaviour for linearized or fully nonlinear equations); — - — -, inviscid linear Navier–Stokes equations ($J = 0$). (*b*) Influence of the initial amplitude of the perturbation velocity ϵ_{2D}: ——, $\epsilon_{2D} = 0.11$ (run 4); ----, $\epsilon_{2D} = 0.011$; — — —, $\epsilon_{2D} = 0.0011$ (run 8).

of $\approx 7 \times 10^{-5}$. Also plotted in figure 6(*a*) is $E(\alpha)$ corresponding to a calculation solving the inviscid Boussinesq equations (long-dash line). A growth rate of 0.07 is found for the perturbation velocity, in agreement with Hazel's (1972) computations. This latter curve also shows that viscosity starts influencing the perturbation growth very early, in less than one Brunt–Väisälä period.

Note that all three curves in figure 6(*a*) start with a higher slope, equal to 0.19 (for the perturbation velocity again). This results from the choice of this perturbation: its vertical dependence at $t = 0$ is the eigenfunction of the Rayleigh equations (without stratification) for the most unstable mode and about a quarter of Brunt–Väisälä period is needed for the stable stratification to influence the fluid motion.

As shown by figure 5, the initial value of $E(\alpha)$ chosen for all calculations presented in this paper is about 10^{-4}, which corresponds to the end of the linear regime, according to figure 6(*a*). We have checked that the behaviour of the flow once nonlinear saturation is reached is qualitatively the same, whether the initial amplitude of the perturbation is equal to ϵ_{2D}, $\epsilon_{2D}/10$ or $\epsilon_{2D}/100$. More precisely, we have found that the maximum vorticity is decreased by only 10% and 18% for the two latter cases respectively compared to the first one (this behaviour being due to the fact that the minimum Richardson number increases with time, both velocity and density profiles broadening). However, the growth rate of the perturbation is so slow that the time at which the saturation of $E(\alpha)$ occurs is strongly dependent upon the initial amplitude of this perturbation. This is illustrated in figure 6(*b*) where $E(\alpha)$ is plotted up to the time when the nonlinear saturation occurs, for the three initial amplitudes mentioned above. Figure 6(*b*) shows that 3000 iterations separate the two first maxima of $E(\alpha)$ while 3600 additional iterations separate the two later ones. This justifies the choice made here for the amplitude of the perturbation, especially because the stage of the flow of interest, during which secondary instabilities grow, occurs well after this nonlinear saturation has been reached.

3.2.3. *Influence of the Reynolds number upon the overall structure of the baroclinic layer*

The minimum value of the Richardson number of the baroclinic layer displayed in figure 3 is always reached at the stagnation point and its smallest value as time elapses, equal to 0.07, is well below the critical value for linear stability. Nevertheless, in accordance with previous numerical studies mentioned in the Introduction, no secondary Kelvin–Helmholtz instability develops at the stagnation point. We define the Richardson number of the baroclinic layer as in Corcos & Sherman (1976):

$$Ri = -J\left[\frac{\partial\rho/\partial z}{\Omega^2}\right], \tag{3.1}$$

Ω being the vorticity of the layer. The value of Ri at the stagnation point will be denoted Ri_S.

The influence of the Reynolds number Re upon the structure of the baroclinic layer is illustrated in figure 7, for Re ranging between 140 and 2600: as Re increases, the thickness of the vorticity layer and of its companion density layer decrease. These two events contribute to increase the vorticity of the flow, the latter through the baroclinic torque. Though Ri_S reaches an absolute minimum value as small as 0.046 at the stagnation point for $Re = 2600$ (figure 7*d*), no instability develops there. (It should be noted that the $Re = 140$ flow is dominated by stabilizing effects, namely stratification and viscosity. However, as discussed in §4.6.2, it will be interesting to compare its dynamics with those of a three-dimensional calculation having the same values of J and Re, which appears to bear a secondary instability.)

In order to address this intriguing stability of the baroclinic layer at its stagnation point, we shall first conduct a quantitative study of the influence of the Reynolds number upon the behaviour of the layer. For this purpose, the theoretical model proposed by Corcos & Sherman (1976) will be used. This model allows a careful study of the structure and dynamics of a baroclinic layer and was developed to reproduce the features of a weakly stratified shear layer obtained by the numerical simulations of Patnaik *et al.* (1976). It was thus tested in this case ($J = 0.03, Re = 25$). To our knowledge, no other validation of this model has been performed since then.

We shall first recall the principles of the model, stressing its underlying physical mechanisms. We shall next compare its predictions to our numerical simulations of a strongly stratified shear layer. This model will then help us to understand why the layer remains stable at the stagnation point.

3.3. *Comparison with the model of Corcos & Sherman (1976)*

3.3.1. *Physics of the model*

In the model of Corcos & Sherman, the dynamics of the baroclinic layer in the neighbourhood of the stagnation point are modelled by the Boussinesq equations written in a frame of reference attached to the layer. The coordinates along the direction of the layer and normal to it are denoted by σ and η respectively and originate from the stagnation point (figure 8). The layer is assumed to be subjected to a pure strain field of uniform and constant strain rate, γ, induced by the vorticity of the large-scale Kelvin–Helmholtz vortices and by the end of the baroclinic layers. An important assumption of the model is that the *local* vorticity of the layer, Ω, can be treated as a passive scalar, in the sense that the velocity field induced by the vorticity of the layer itself plays no role in the advection of this vorticity (and of its companion density field);

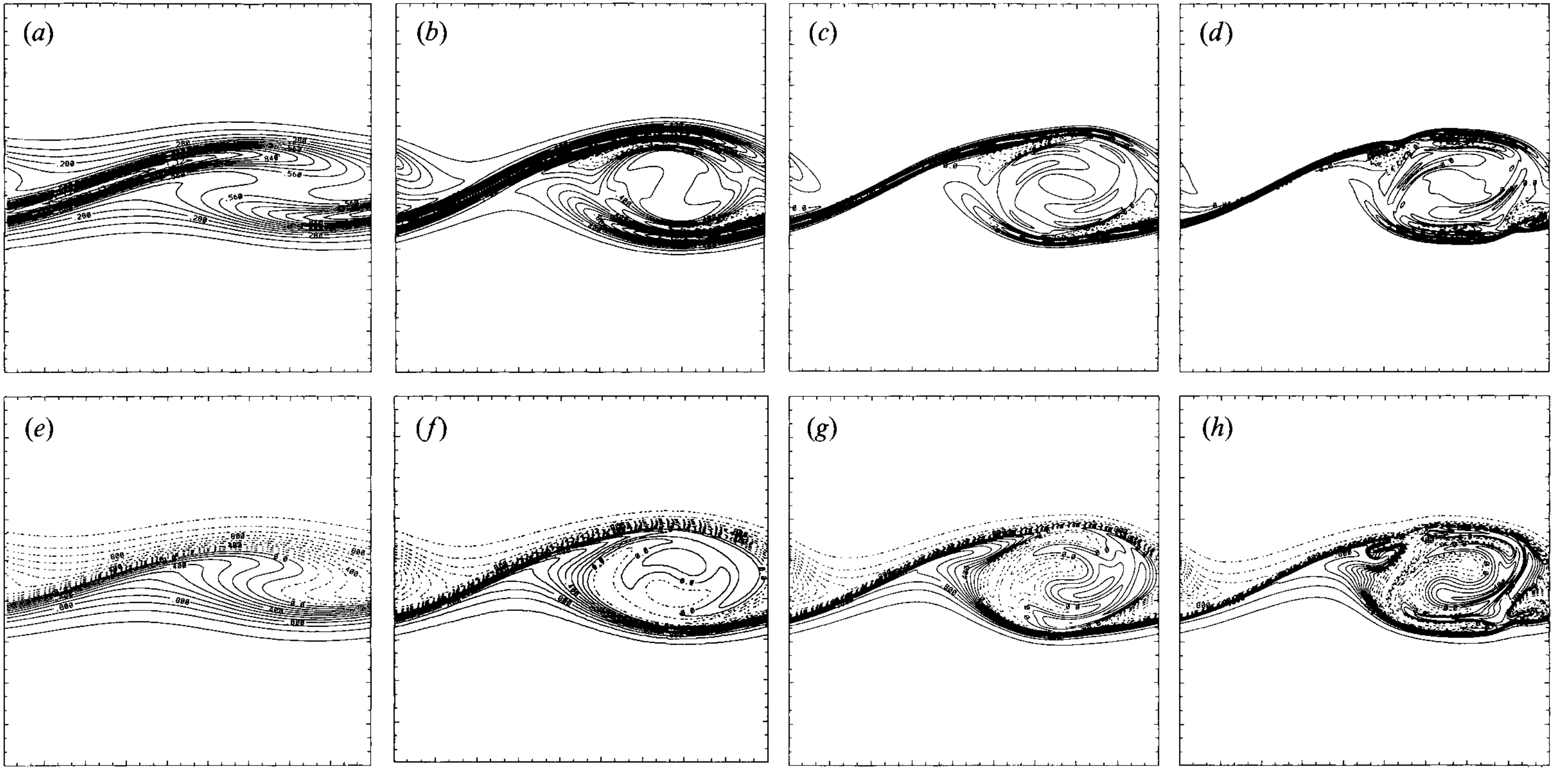

FIGURE 7. Influence of the initial Reynolds number *Re* upon the structure of the flow at the time the vorticity reaches an absolute maximum Ω_{max}. This maximum is located at the stagnation point of the vorticity layer. Ri_s defined by (3.1), is the Richardson number at this location. *d* is the distance between contour levels. (*a–d*) Contours of constant vorticity. (*a*) $Re = 140$, $Ri_s = 0.20$, $\Omega_{max} = 1.19$, $d = 0.07$ (run 2); (*b*) $Re = 400$, $Ri_s = 0.12$, $\Omega_{max} = 2.3$, $d = 0.1$ (run 3); (*c*) $Re = 1000$, $Ri_s = 0.07$, $\Omega_{max} = 3.6$, $d = 0.3$ (run 4); (*d*) $Re = 2600$, $Ri_s = 0.046$, $\Omega_{max} = 6$, $d = 0.5$ (run 7). (*e–h*) Contours of constant density corresponding to (*a–d*). $d = 0.1$.

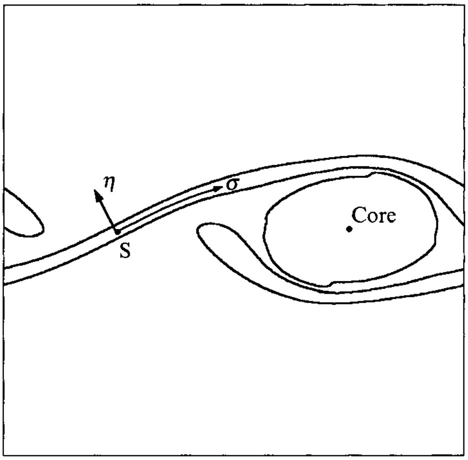

FIGURE 8. Local frame of reference (σ, y, η) attached to the baroclinic layer (the y spanwise axis has not been represented for clarity). S is the stagnation point of the baroclinic layer.

only the outer strain field is responsible for this advection. The vorticity and density fields are assumed to be independent of σ. Similarity solutions for these two fields can then be tested, which solely depend upon η/δ and η/δ_ρ respectively, δ and δ_ρ being the half-thickness of the vorticity layer and companion density layer. For such solutions, the model predicts the existence, at large time, of a stationary regime which is characterized by two local equilibria: (i) along η, the transport by the strain field opposes diffusive effects; (ii) along σ, the outward advection by the strain field (towards the Kelvin–Helmholtz vortices) balances the local production of vorticity by the baroclinic torque. The first equilibrium yields a constant thickness of the baroclinic layer, an estimate of which can be obtained by writing that the characteristic time scales of strain and diffusion are of the same order: $1/\gamma \sim Re\,\delta_\infty^2$, for the vorticity layer and $1/\gamma \sim Pr\,Re\,\delta_{\rho\infty}^2$, for the companion density layer. The expressions for the asymptotic half-thicknesses δ_∞ and $\delta_{\rho\infty}$ predicted by the model are

$$\delta_\infty = \left(\frac{\pi}{2\gamma Re}\right)^{1/2} \quad \text{and} \quad \delta_{\rho\infty} = \frac{\delta_\infty}{Pr^{1/2}}. \tag{3.2}$$

The second local equilibrium leads to a constant velocity difference across the layer. This can be seen directly by considering the budget equation for the vorticity averaged over the layer width, $\mathscr{L}$ say, within a slice of length $\mathrm{d}\sigma$ of this layer:

$$\frac{\partial}{\partial t}\int_{\mathscr{L}} \Omega\,\mathrm{d}\eta = J\int_{\mathscr{L}} \frac{\partial\rho}{\partial x}\mathrm{d}\eta + \left[\int_{\mathscr{L}} u_\sigma \Omega\,\mathrm{d}\eta\right]_\sigma - \left[\int_{\mathscr{L}} u_\sigma \Omega\,\mathrm{d}\eta\right]_{\sigma+\mathrm{d}\sigma}, \tag{3.3}$$

where u_σ is the component along σ of the total velocity field. (An estimate of $\mathscr{L}$ will be given in §3.3.2 below.) Using $\eta = -\sin(\theta)\,x$, θ being the angle that the layer makes with the horizontal at the stagnation point, yields

$$\frac{\partial}{\partial t}\int_{\mathscr{L}} \Omega\,\mathrm{d}\eta = J\sin(\theta)\,\Delta\rho_L - \frac{\partial}{\partial\sigma}\int_{\mathscr{L}} u_\sigma \Omega\,\mathrm{d}\eta. \tag{3.4}$$

$\Delta\rho_L$ is the (positive) density difference across the vorticity layer when this layer is crossed from below to above over the distance $\mathscr{L}$. The velocity component u_σ is made up of two contributions: the component of the pure strain field, $\gamma\sigma$, plus the velocity component induced by the layer itself. We shall assume that the net flux associated with this latter contribution vanishes; this is true if the vorticity distribution is symmetric with respect to the $\eta = 0$ axis. It will be necessary to check this assumption in the present case of a strongly stratified shear flow, because the intense vorticity of the layer, if slightly asymmetrically distributed, would induce an appreciable net flux compared to the pure strain contribution. Under this assumption, (3.4) can be solved easily and yields the temporal evolution of the velocity difference across the layer over the distance $\mathscr{L}$:

$$\Delta V(t) = \int_{\mathscr{L}} \Omega \, \mathrm{d}\eta(t) = A \, \mathrm{e}^{-\gamma t} + J \sin(\theta) \frac{\Delta\rho_L}{\gamma}. \tag{3.5}$$

A is a constant imposed by the initial conditions (the 'initial' time being the one at which the strain rate reaches a constant value). The derivation of (3.5) assumes also that the product $\sin(\theta)\,\Delta\rho_L$ is constant, or at least that the main contribution to the temporal variation of $\Delta V(t)$ in (3.5) stems from the exponential term. This assumption will have to be checked also. For a weakly stratified shear layer, the numerical computations of Patnaik *et al.* (1976) show that $\Delta\rho_L$ is the total density difference at the horizontally oriented boundaries (i.e. $\Delta\rho_L = \Delta\rho$). By contrast, in the present case where the fluid is strongly stratified, $\Delta\rho_L$ has to be determined from the numerical simulations (see figure 7). As time goes to infinity, the velocity difference across the layer reaches the asymptotic value

$$\Delta V_\infty = J \sin(\theta)\, \Delta\rho_L / \gamma. \tag{3.6}$$

We need to recall the similarity solutions for the vorticity and density fields predicted by the model of Corcos & Sherman:

$$\rho(\eta, t) = -\frac{\Delta\rho_L}{2} \operatorname{erf}\left(\frac{\pi^{1/2}}{2} \frac{\eta}{\delta_\rho(t)}\right) \quad \text{and for } Pr = 1, \quad \Omega(\eta, t) = \frac{\Delta V(t)}{2\delta(t)} \exp\left[-\frac{\pi}{4}\left(\frac{\eta}{\delta(t)}\right)^2\right]. \tag{3.7}$$

These expressions will provide the definitions of $\delta(t)$ and $\Delta\rho_L$ which will be used to compute numerically these two quantities. Note that $\delta(t)$ is half the vorticity thickness of the baroclinic layer. Using (3.2) and (3.6), the asymptotic value of the vorticity of the layer at the stagnation point ($\eta = 0$) can easily be infered from (3.7):

$$\Omega_\infty = \frac{1}{(2\pi)^{1/2}} J \, Re^{1/2} \frac{\Delta\rho_L \sin(\theta)}{\gamma^{1/2}}. \tag{3.8}$$

Finally, a main implication of the model is the derivation of an analytic expression for the Richardson number at the stagnation point of the layer when the asymptotic stationary regime is reached, Ri_∞. The expression for Ri_∞ is obtained from (3.1), using (3.8) and (3.7) for $\eta = 0$,

$$Ri_\infty = (2\pi)^{1/2} \frac{Pr^{1/2}}{J \, Re^{1/2}} \frac{\gamma^{3/2}}{\Delta\rho_L} \frac{\cos(\theta)}{\sin^2(\theta)}. \tag{3.9}$$

(Note that Ri_∞ does not explicitly depend upon the Prandtl number, J being proportional to $Pr^{1/2}$.)

The test of this model against our numerical simulations has to be done in two steps. We first have to compute the physical parameters characterizing the baroclinic layer (besides those characterizing the flow: J, Re and Pr), which are the strain rate γ, its angle with the horizontal θ and the density difference across the layer $\Delta\rho_L$. Then, we shall test the asymptotic theoretical expressions for the thickness of the layer (3.2), the velocity difference across the layer (3.6), and the vorticity and local Richardson number at its stagnation point (3.8) and (3.9) respectively. In what follows, the asymptotic equilibrium state of the layer will be assumed to be the state of maximum vorticity (over space and time). According to figure 15(*a*), this state is reached at $t \approx 52$, provided that $Re \geqslant 400$. All comparisons with asymptotic theoretical predictions will thus be made at $t = 52$, the values of γ, θ and $\Delta\rho_L$ being taken at that time as well.

3.3.2. *Numerical computation of the physical parameters characterizing the baroclinic layer*

Outer velocity field acting upon the layer. We define numerically the $\eta = 0$ axis by the loci of the baroclinic layer where the vorticity is maximum. A locally orthogonal coordinate system (σ, η) can then be defined anywhere along this line of maximum vorticity loci, originating at a given point of this line. In the present case, we shall only need to define this coordinate system at the stagnation point: the dependence on η will only be examined across this particular locus of maximum vorticity. By contrast, the dependence on the curvilinear coordinate σ will be computed away from the stagnation point, along the curved line of maximum vorticity loci.

We first need to check that the outer velocity field acting upon the baroclinic layer in the neighbourhood of the stagnation point is a pure strain field with uniform and constant strain rate. Figure 9(*a*) displays the component of the total velocity field along the $\eta = 0$ axis for run 4 ($Re = 1000$) as a function of σ, at $t = 39$. A linear dependency is obtained, with slope ≈ 0.155. The component of the total velocity field along the $\sigma = 0$ axis is plotted in figure 9(*b*) versus η, at the same time; a linear dependency with same slope as in figure 9(*a*) is obtained. These results are compatible with the assumption that the outer velocity field acting upon the layer at that time is a pure strain field, with uniform strain rate. The same curves are plotted at $t = 52$ (figure 9*c, d*), at the time the layer is assumed to reach an equilibrium state. The same linear dependency is observed, but note that the slope (i.e. the strain rate) has increased by about 16%, being now equal to 0.18. This point will be discussed below.

The model of Corcos & Sherman also assumes that the vorticity Ω and density of the layer are independent of σ. We have checked that, at the time the layer reaches an equilibrium state, Ω varies by less than 3% for $Re = 2000$, and by 4% for $Re = 400$, over a distance from the stagnation point equal to one height of the streamwise extent of the numerical domain. For the density field, figure 7 clearly shows that, in the neighbourhood of the stagnation point, constant contours of the density are close to straight lines along the direction of the layer (i.e. have a very large radius of curvature compared to the layer thickness). The fact that the vorticity and density of the layer are quasi-independent of σ, and that the layer is nearly straight, implies that the velocity field associated with the layer is close to a parallel flow. This justifies the main assumption of the model that the vorticity and density of the layer are passively advected by the strain field.

The temporal behaviour of γ is displayed in figure 10 for runs 2–7. In this figure as well as in the remainder of this paper, γ is computed using the analytic expression (Dritschel *et al.* 1991, p. 660)

$$\gamma = \boldsymbol{t} \cdot \boldsymbol{\nabla u} \cdot \boldsymbol{t} \quad \text{with} \quad \boldsymbol{t} = -\boldsymbol{i}_y \times \boldsymbol{n} \quad \text{and} \quad \boldsymbol{n} = \boldsymbol{\nabla}\omega / |\boldsymbol{\nabla}\omega|; \tag{3.10}$$

$\boldsymbol{\nabla u}$ is the second-order tensor of the velocity derivatives and $\boldsymbol{\nabla}\omega$, the gradient of the vorticity of the flow. $\boldsymbol{t}$ is a unit vector parallel to the vorticity contours having larger

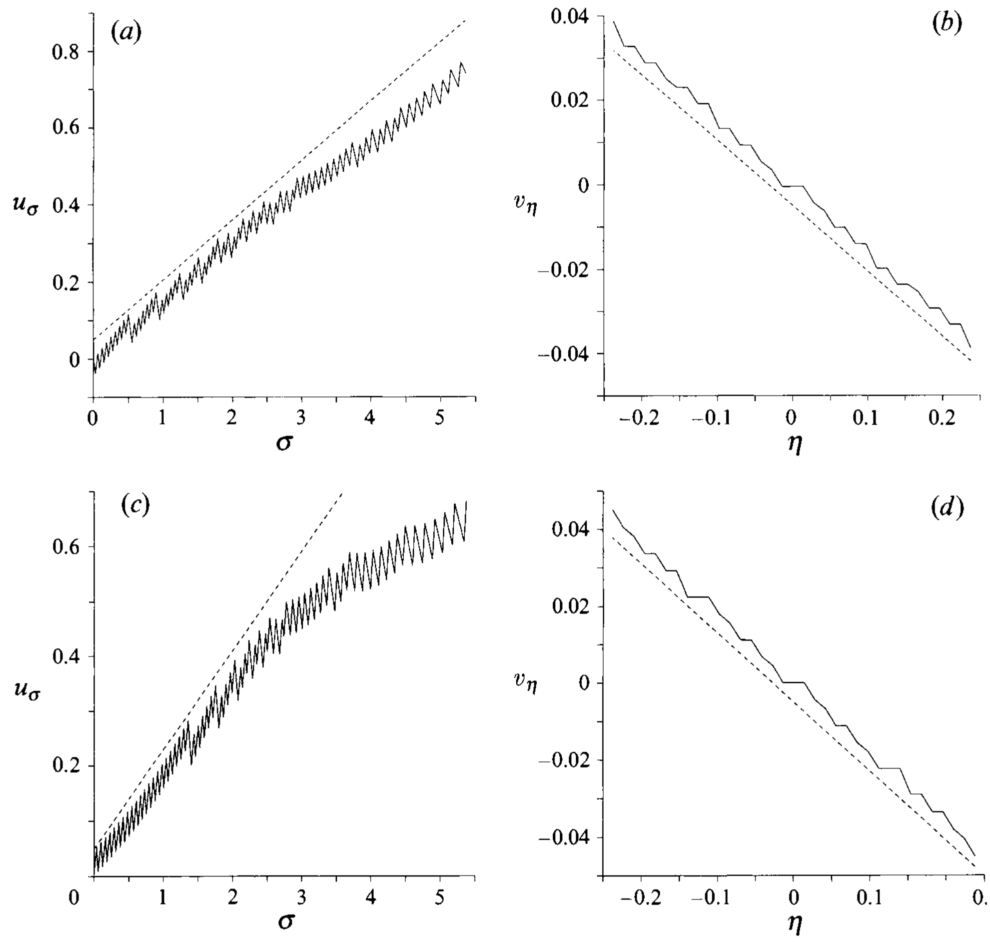

FIGURE 9. Run 4. (*a*) Component along the direction of the layer ($\eta = 0$) of the total velocity field, u_σ, versus σ, at $t = 39$; (*b*) Component perpendicular to the direction of the layer ($\sigma = 0$) of the total velocity field, v_η, versus η, at the same time. A dashed line of slope 0.155 is drawn. (*c*, *d*) Analogous to (*a*, *b*) respectively, at $t = 52$. A dashed line of slope 0.18 is drawn.

vorticity on the right. Thus, in the neighbourhood of the baroclinic layer, γ is the strain rate along this layer. Since γ is undefined at the stagnation point of the layer, its value at location ($\sigma = 0, \eta = \delta(t)$) will be computed instead, with $\delta(t)$ defined by (3.7).

Figure 10 shows that, as the primary instability develops, γ increases from a small but non-zero value (due to the initial two-dimensional perturbation) and reaches a regime, between $t \approx 20$ and $t \approx 40$, where it is about constant. Note that γ is almost Reynolds-number independent, especially for $Re \geqslant 1000$. The reason is that the outer velocity field acting upon the layer is induced by the Kelvin–Helmholtz vortex (and the surrounding end part of the baroclinic layer), which is a large-scale structure. However, this structure is not stationary: the end parts of the baroclinic layer are advected by the local flow, which makes the size of the Kelvin–Helmholtz vortex increase. This may account for the small increase of γ (by 16%), which is observed from $t \approx 40$: γ is indeed roughly proportional to the circulation of the velocity field around this large-scale structure. Figure 9(*c*, *d*) show that, during this stage of the flow, the outer velocity acting upon the layer still remains of the pure strain type. Note that the slope of 0.18

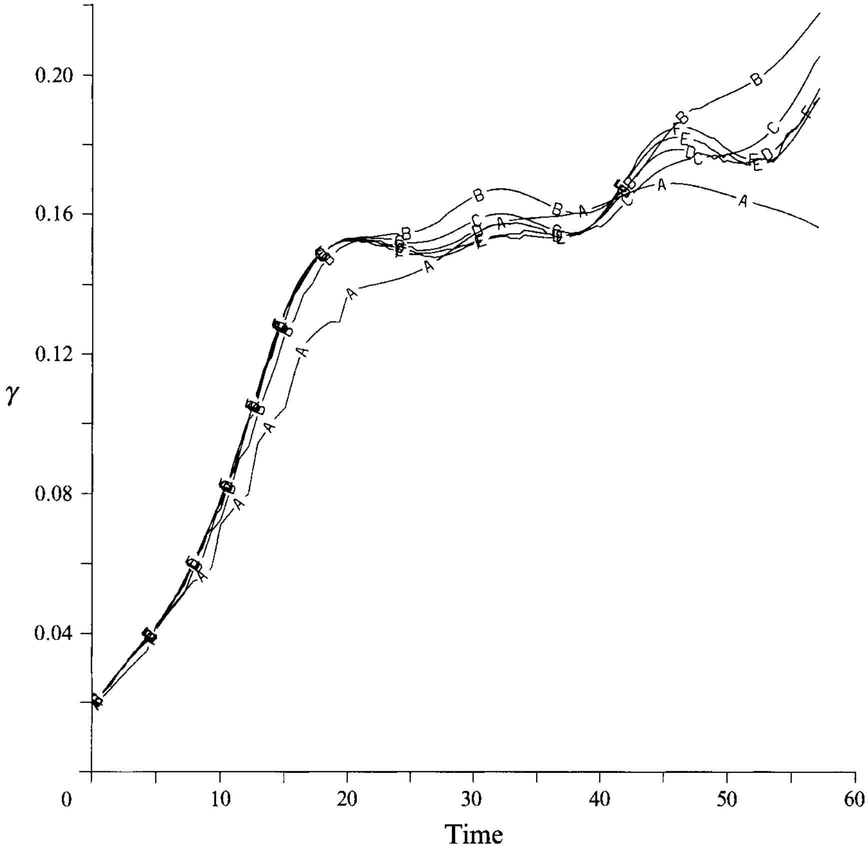

FIGURE 10. Temporal evolution of the strain rate γ at location ($\sigma = 0, \eta = \delta(t)$), with $\delta(t)$ defined by (3.7). A, $Re = 140$; B, $Re = 400$; C, $Re = 1000$; D, $Re = 1500$; E, $Re = 2000$; F, $Re = 2600$. (Runs 2–7.)

displayed in these figures is in agreement with the strain rate at that time ($t = 52$) plotted in figure 10 (the same remark holds for $t = 39$, with $\gamma = 0.155$).

Angle of the layer with the horizontal. The temporal behaviour of the angle θ that the baroclinic layer makes with the horizontal at the stagnation point is plotted in figure 11 for different initial Reynolds numbers. θ appears to be independent of Re, at least for $Re \geqslant 400$. The same argument as for the strain rate γ can be invoked, since θ results from the nonlinear development of the large-scale Kelvin–Helmholtz vortex.

Density difference across the layer. The density difference across the layer $\Delta\rho_L$ is defined by (3.7): it is twice the value of the density at the distance along η (from the stagnation point) where the error function attains its asymptotic value. For $\eta/\delta(t) = 3$, $\rho(\eta) = \Delta\rho_L/2$ within 0.2%. This is good enough precision for the present numerical comparison with the theory and 'infinite' distance from the stagnation point will thus be assumed to be reached at $3\delta(t)$. This provides an estimate for the overall layer thickness $\mathscr{L}$ defined in §3.3.1: $\mathscr{L} = 6\delta(t)$. The values of $\Delta\rho_L$ computed numerically (at a distance $\pm 3\delta(t)$ from the stagnation point) are indicated in table 1 for runs 2–7, at $t = 52$. $\Delta\rho_L$ appears to be quasi-independent of the Reynolds number, as is the angle θ. Moreover, we have found that this quantity varies by 20% at most between $t \approx 30$ and $t = 58$.

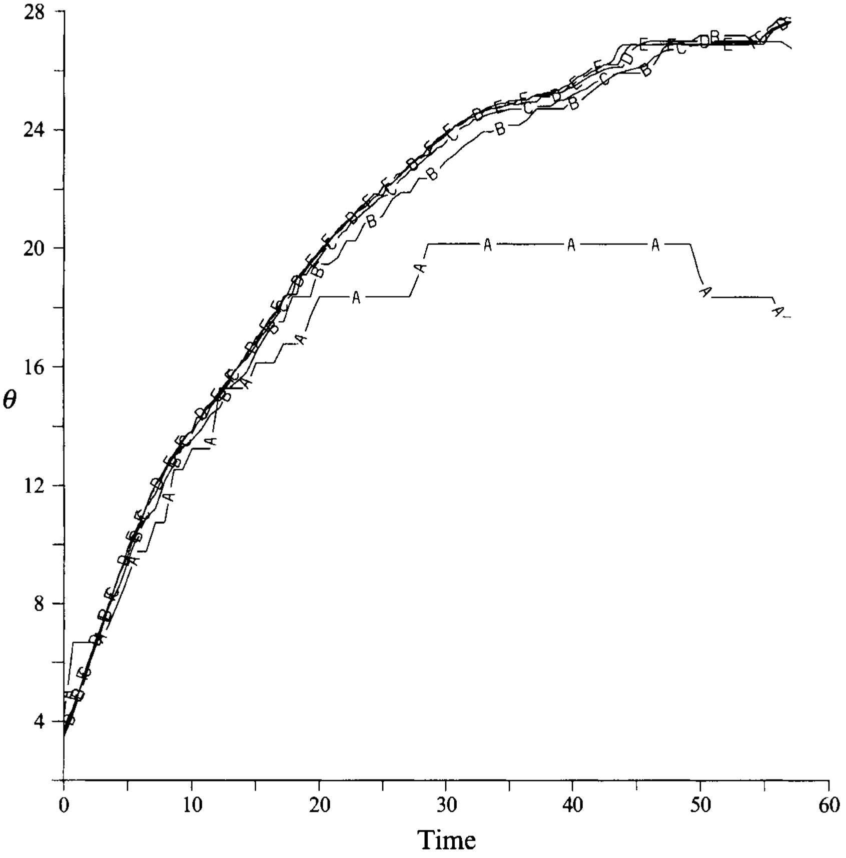

FIGURE 11. Temporal evolution of the angle θ (in degrees) that the baroclinic layer makes with horizontal at the stagnation point. A, $Re = 140$; B, $Re = 400$; C, $Re = 1000$; D, $Re = 1500$; E, $Re = 2000$; F, $Re = 2600$. (Runs 2–7.)

3.3.3. *Test of the model*

Thickness of the layer. The thickness of the layer $\delta(t)$ is defined numerically by (3.7): it is the distance η from the stagnation point at which the vorticity Ω is equal to $e^{-\pi/4}\Omega(\eta = 0, t)$. $\delta(t)$ is plotted versus time for runs 2–7 in figure 12(*a*). Two regimes can be clearly distinguished (for $Re \geqslant 400$). An inviscid regime first sets in, up to $t \approx 20$, which is associated with the development of the primary Kelvin–Helmholtz instability, during which the evolution of the layer thickness is controlled by the growing strain field. Once the scale at which viscous diffusion is active is reached, an equilibrium quickly occurs, formalized by (3.2). This can be seen in figure 12(*b*) where $\delta(t = 52)$ computed numerically and δ_∞ defined by (3.2) are plotted versus the initial Reynolds number using a log–log scale. Since $\gamma(t = 52)$ is almost independent of Re (see figure 10), the theoretical values follow the $Re^{-1/2}$ decay law quite closely. Moreover, good agreement is found with the values computed numerically: figure 12(*b*) shows that, for $Re \geqslant 400$, both numerical and theoretical values differ by 20% at most.

Velocity difference across the layer. The derivation of equation (3.5), which yields the asymptotic expression for the velocity difference across the layer, assumes that the net flux of vorticity along the layer results solely from the advection by the component along σ of the pure strain field, $\int_{\mathscr{L}} \gamma\sigma\Omega \, d\eta$. This assumption is verified in figure 13: the total flux of vorticity along σ, $\int_{\mathscr{L}} u_\sigma \Omega \, d\eta$ is found to be in good agreement with the pure

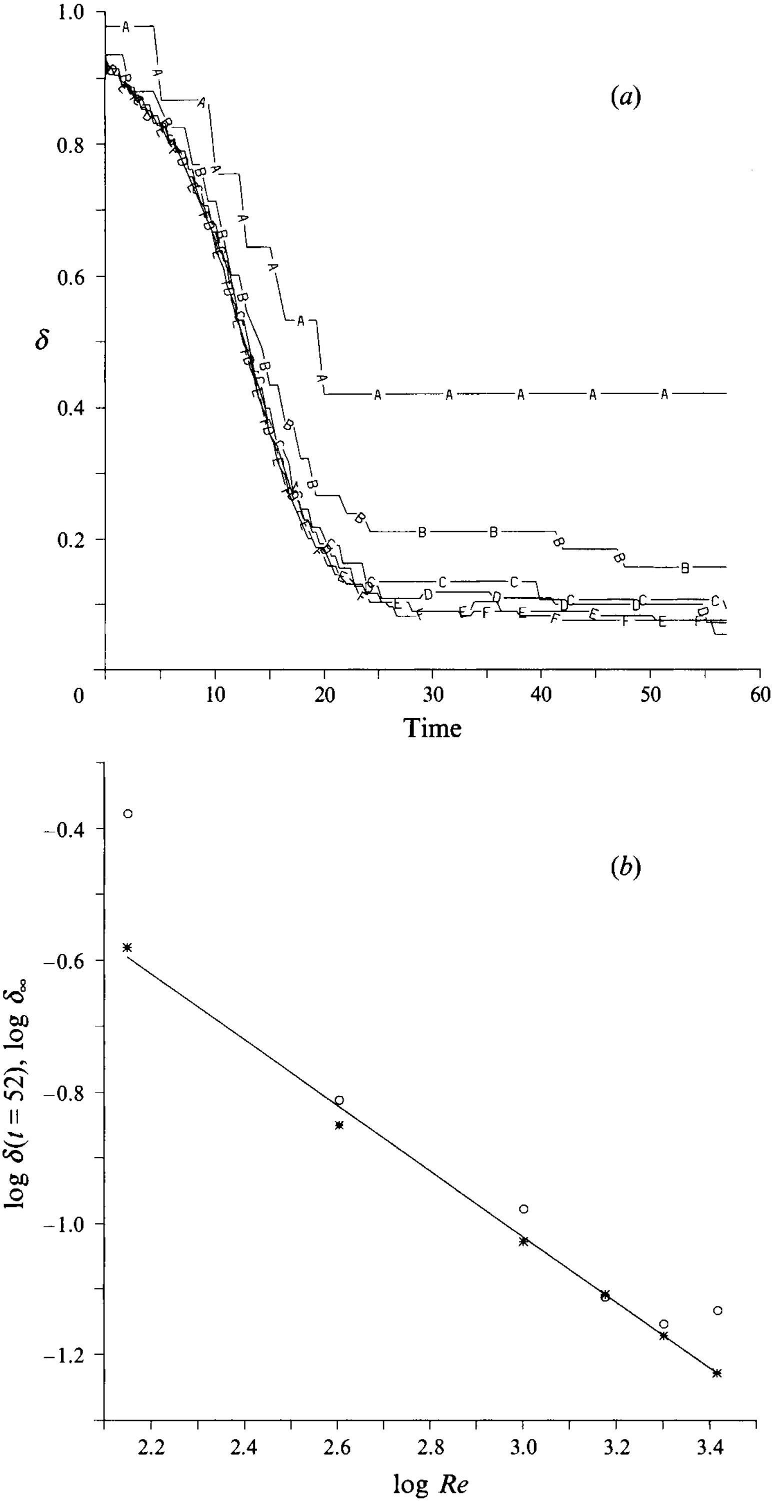

FIGURE 12. Half-thickness of the vorticity layer $\delta(t)$, defined by (3.7). (*a*) Versus time: A, $Re = 140$; B, $Re = 400$; C, $Re = 1000$; D, $Re = 1500$; E, $Re = 2000$; F, $Re = 2600$. (Runs 2–7.) (*b*) Versus Reynolds number: ○, values computed numerically at $t = 52$; *, theoretical values δ_∞ given by (3.2) at the same time. A log-log scale base 10 is used. The slope of the straight line is $-\frac{1}{2}$.

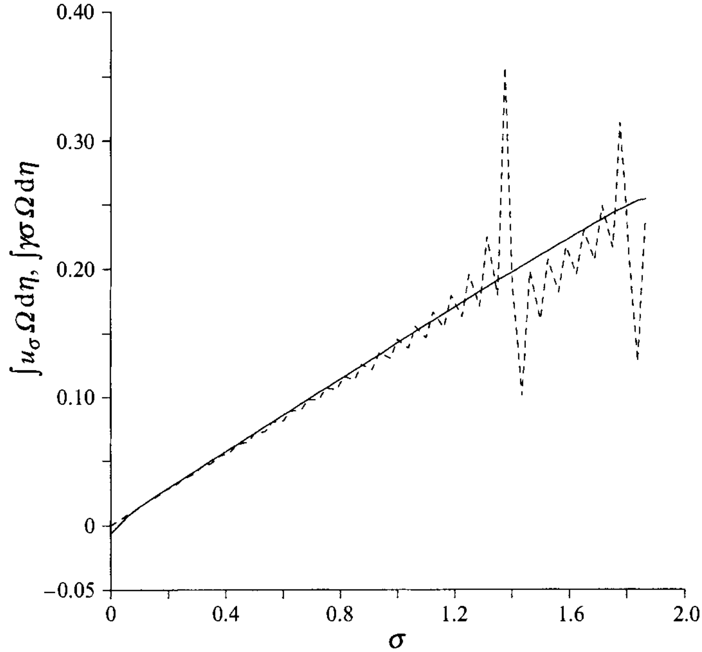

FIGURE 13. Run 4 ($Re = 1000$) at $t = 52$. Net flux along the layer of the vorticity Ω advected by the total velocity field, $\int u_\sigma \Omega \, d\eta$ (——) and by the pure strain field, $\int \gamma\sigma\Omega \, d\eta$ (– – – –). σ and η are defined in figure 8, γ is the strain rate (see figure 10).

strain contribution alone. For the second assumption used in the derivation of (3.5), we have checked that $\sin(\theta)\,\Delta\rho_L$ varies by 40% at most for $20 \leqslant t \leqslant 52$ whatever Re, while the exponential term decreases by a factor ≈ 100 during the same time, both terms being of the same order at the 'initial' time $t = 20$. (Computation of A in (3.5) at this initial time yields a positive value of order 1.)

The asymptotic setting-up of a constant velocity difference across the layer is now examined. This velocity difference is computed by summing Ω over a distance $\mathscr{L}$ of $6\delta(t)$ across the layer (see §3.3.2). The temporal evolution of $\Delta V(t) = \int_{\mathscr{L}} \Omega \, d\eta$ is plotted in figure 14(*a*) for runs 2–7. At $t = 0$, this velocity difference is close to 2, which is the velocity difference between the horizontally oriented boundaries. For $Re \geqslant 400$, $\Delta V(t)$ sharply decreases from $t \approx 13$, at about the same rate whatever Re: just as for $\delta(t)$, the evolution of $\Delta V(t)$ is controlled by the growing strain field during this sharp decrease, in agreement with (3.5). A plateau is then reached, whose value is almost independent of the Reynolds number, especially at large times (for $t \geqslant 40$). This latter result is consistent with the fact that these velocity differences are equal at $t = 0$ and decrease at the same rate, independently of Re. $\Delta V(t = 52)$ computed numerically is tested against its theoretical expression (3.6) at the same time in figure 14(*b*). Very good agreement is found, the relative difference decaying from 21% (for $Re = 400$) down to 9% (for $Re = 2600$). Note that, for $Re \geqslant 400$, both theoretical and numerical values become almost independent of the Reynolds number, because γ, $\Delta\rho_L$ and θ also behave quasi-independently of this parameter.

Vorticity at the stagnation point of the layer. Though the vorticity at the stagnation point of the layer, denoted Ω_s hereafter, is simply the ratio of $\Delta V(t)$ to $2\delta(t)$, whose behaviour and asymptotic values have been shown to be very well predicted by the model of Corcos & Sherman, it is still interesting to examine its temporal evolution for

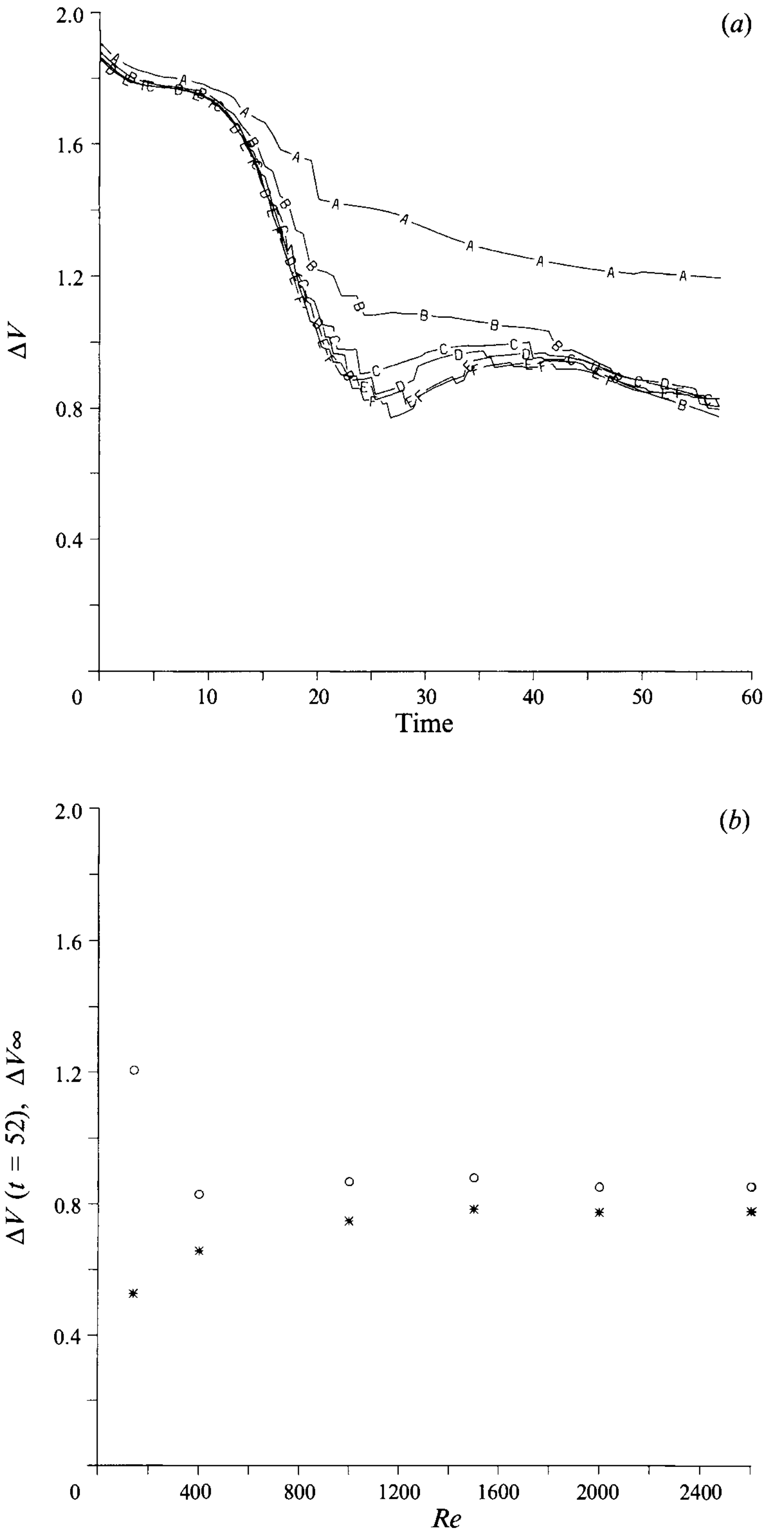

FIGURE 14. Velocity difference ΔV across the layer. (*a*) Versus time: A, $Re = 140$; B, $Re = 400$; C, $Re = 1000$; D, $Re = 1500$; E, $Re = 2000$; F, $Re = 2600$. (Runs 2–7.) (*b*) Versus Reynolds number: ○, values computed numerically at $t = 52$; *, theoretical values ΔV_∞ given by (3.6) at the same time.

different Reynolds numbers. These evolutions are displayed in figure 15(*a*). As already noted, two regimes appear clearly, especially for $Re \geqslant 1000$: the temporal growth of Ω does not depend upon viscous effects up to $t \approx 20$ but curves strongly separate from this time, essentially because of the influence of the Reynolds number upon the layer thickness: the baroclinic production rate of the vorticity in the layer being proportional to $J \sin(\theta) \Delta\rho_L / \delta$, this rate increases with decaying layer thickness ($\sin(\theta) \Delta\rho_L$ being approximately constant). Since the vorticity is advected during the same time at a constant rate γ, whatever Re, the equilibrium vorticity increases with Re but is reached at the same time, at $t \approx 52$. Equilibrium values of the vorticity are plotted versus Re in figure 15(*b*) (for $Re \geqslant 400$) and compared with the theoretical expression (3.8) at the same time. Remarkable agreement is obtained, the relative difference being always less than 4.4%. However, the $Re^{1/2}$ law predicted by the model is only verified for $Re \geqslant 1000$, owing to the lower value of $\Delta\rho_L$ below this Reynolds number.

Finally, it is interesting to plot γ and Ω as functions of η across the stagnation point at $t = 52$, for $Re = 2000$ (figure 16). Note the very sharp variation of Ω which contrasts with the quasi-uniform behaviour of γ across the layer. This difference in behaviour is all the more striking since the Reynolds number is higher.

Richardson number at the stagnation point of the layer. We first check that theoretical expression (3.7) for the density profile accurately predicts the profile numerically computed. (There is no doubt that the vorticity profile of the layer is well predicted by the model, according to figures 12*b* and 15*b*.) Both density profiles are compared in figure 17, for $Re = 1000$ at $t = 52$: remarkable agreement is obtained.

The temporal evolution of the Richardson number at the stagnation point of the layer, Ri_s, is plotted in figure 18(*a*). For $Re \geqslant 1000$, Ri_s constantly decreases from $t \approx 13$, at about the same rate until $t \approx 25$ (as the layer thickness does, see figure 12*a*). A plateau is reached from $t \approx 40$, whose value decreases with increasing Reynolds number, as expected. $Ri_s(t = 52)$ is plotted versus Re in figure 18(*b*) (for $Re \geqslant 400$) and compared to its theoretical counterpart Ri_∞. Very good agreement is obtained, especially for $Re \geqslant 1000$. Note that, in addition, the $Re^{-1/2}$ decay law is well verified.

As already noted in §3.2.3, Ri_∞ reaches a value as low as 0.046 for $Re = 2600$. We examine now why the stagnation point of the baroclinic layer remains stable.

3.4. *Influence of the outer strain field on the stability of the baroclinic layer*

An heuristic argument can be proposed to account for the persistent stability of the baroclinic layer in the neighbourhood of its stagnation point, which is based upon the outer strain field acting upon the layer. Indeed, this strain field compresses the layer along η, thereby reducing the growth rate of any perturbation, while its component along σ stretches any wavelength along that direction, so that the range of stable wavelengths may eventually be reached.

Such an idea has been given a theoretical framework by Dritschel *et al.* (1991) in the unstratified and inviscid case, for a strip of uniform vorticity subjected to a strain field of constant strain rate. In this situation, the thickness of the vorticity strip decreases exponentially with time, so that perturbations always eventually decay (their growth rate vanishing as their wavenumber goes exponentially to zero). A linear stability analysis of the vorticity layer and its outer velocity field (which together form a time-dependent basic flow in this case) is conducted, which shows that transient growth of a perturbation is possible, depending upon the ratio of the strain rate γ to the layer vorticity Ω. When γ/Ω is greater than 0.25, no amplification of the perturbation occurs, but the perturbation is only amplified by a factor 3 (before decaying) when γ/Ω is as small as 0.065. Nonlinear simulations using a contour dynamics method are also

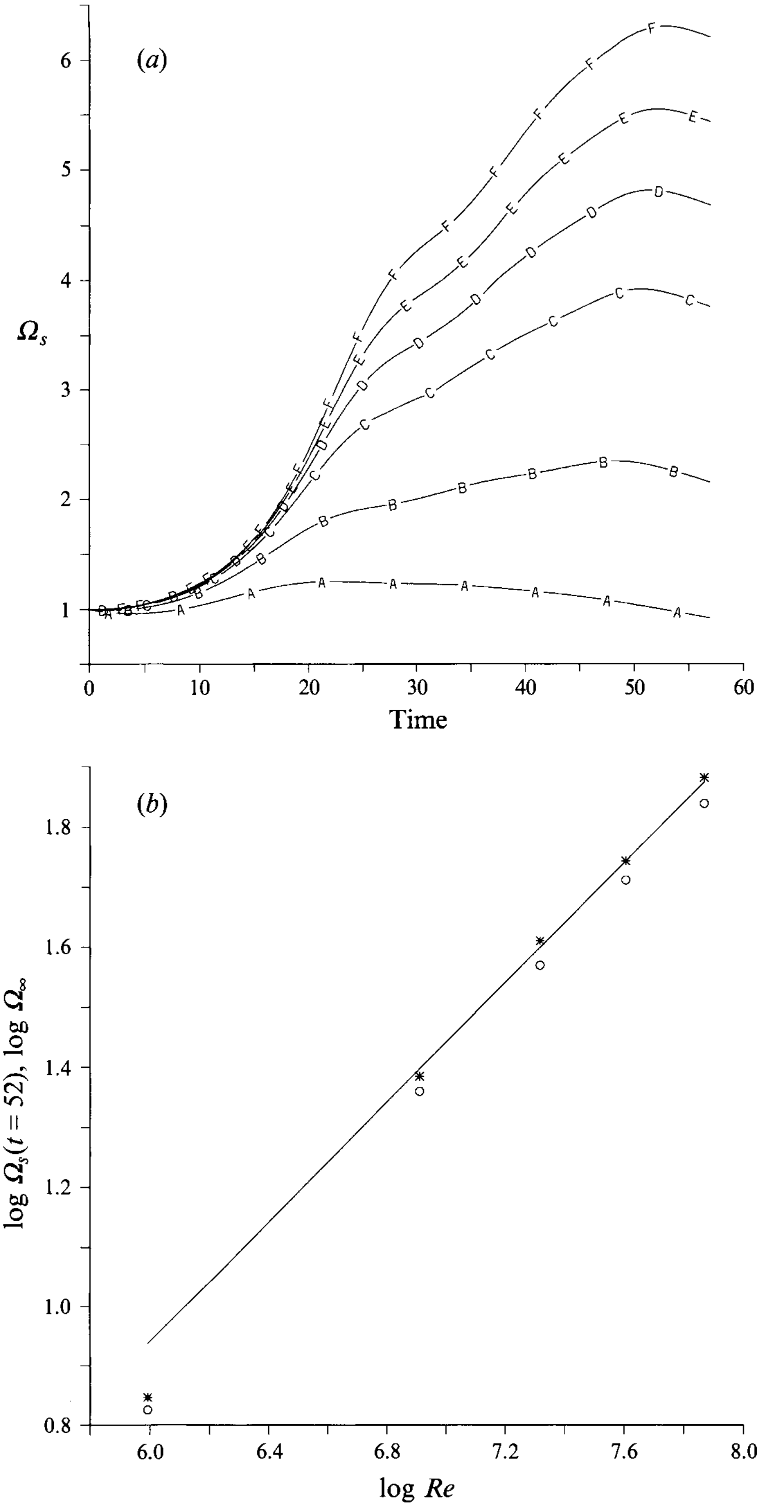

FIGURE 15. Vorticity at the stagnation point of the layer, Ω_s. (*a*) Versus time: A, $Re = 140$; B, $Re = 400$; C, $Re = 1000$; D, $Re = 1500$; E, $Re = 2000$; F, $Re = 2600$. (Runs 2–7.) (*b*) Versus Reynolds number, for $Re \geqslant 400$: ○, values computed numerically at $t = 52$; *, theoretical values Ω_∞ given by (3.8) at the same time. A log-log scale base 10 is used. The slope of the straight line is $\frac{1}{2}$.

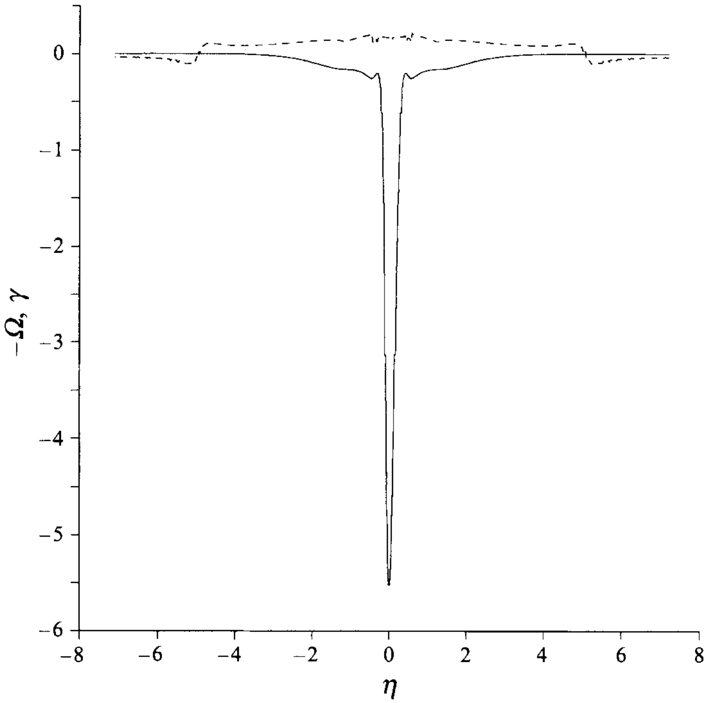

FIGURE 16. Run 6 ($Re = 2000$) for $t = 52$. Vorticity of the layer Ω (——) and rate of strain γ (– – – –) as functions of η for $\sigma = 0$. ($-\Omega$ has been represented for clarity.) See figure 8 for the definition of coordinates σ and η.

presented, which show that the threshold value of γ/Ω over which significant amplification occurs actually strongly depends upon the initial amplitude of the perturbation.

Though the vorticity layers considered in the present study are continuous, stably stratified and viscous diffusion is active, it is still of interest to examine whether Dritschel *et al.*'s main result, namely that even a weak strain can prevent the instability from strongly amplifying, may help in interpreting our results. For this purpose, we have computed the key parameter γ/Ω at the stagnation point of the baroclinic layer, referred to as γ/Ω_s hereafter, for the numerical simulations described in the previous section (runs 2–7 in table 1). γ/Ω_s is plotted in figure 19 (as already noted in §3.3.2, the value of γ at location ($\sigma = 0, \eta = \delta(t)$) has actually been used). The temporal evolutions of γ and Ω_s have been shown in figures 10 and 15(a) respectively. The existence of two different successive regimes, inviscid and strongly Reynolds-number dependent, strikingly appears in figure 19. For $t \geqslant 15$, γ/Ω_s decreases with increasing time and Reynolds number (except for $Re = 140$) and, for $Re \geqslant 1000$, reaches a plateau. Though values as small as 0.045 for $Re = 1000$, 0.031 for $Re = 2000$ and 0.027 for $Re = 2600$ are found, no instability develops at the stagnation point. The reason is very likely that the stable stratification contributes an additional stabilizing effect, quantified by the small but non-zero value of the Richardson number at the stagnation point of the layer.

Within the framework of Dritschel *et al.*'s study, these results thus show that even a value of γ/Ω_s as small as 0.027 with $Ri_s = 0.046$ (for $Re = 2600$) would be enough to prevent the instability from amplifying. The smallness of these values would be consistent with Dritschel *et al.*'s findings. Support for the validity of this approach will

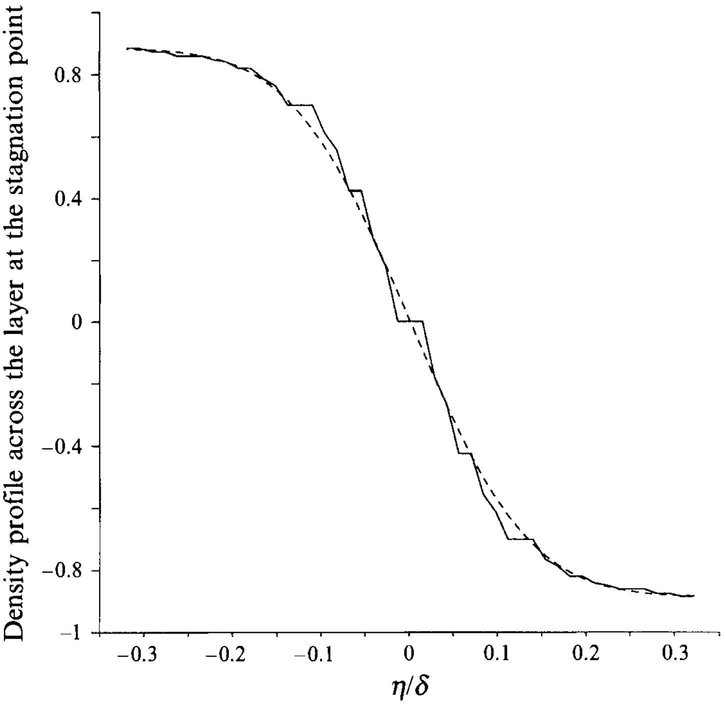

FIGURE 17. Run 4 ($Re = 1000$) at $t = 52$. Density profile across the layer $\rho(\sigma = 0, \eta)$ versus η/δ; δ is half the thickness of the layer at $t = 52$ (see figure 12): ——, numerical computation; ----, theoretical prediction (3.7) by Corcos & Sherman's model.

be provided in §4.4: threshold values for γ/Ω_s and Ri_s below which a secondary instability may occur will be proposed on an empirical basis.

4. Secondary instabilities in a two-dimensional baroclinic layer

4.1. *Development of secondary instabilities in a shear layer with one Kelvin–Helmholtz vortex*

A secondary instability starts developing in the baroclinic layer from $t \approx 44$ and for $Re \geqslant 1500$. This instability does not develop in the neighbourhood of the stagnation point of the baroclinic layer and is not of the Kelvin–Helmholtz type. This unstable evolution is now described for $Re \geqslant 2000$.

Figures 20(a, j) respectively display the vorticity and density fields of the baroclinic layer just before the growth of the secondary instability becomes visible. Note the symmetry of the flow about the stagnation point of the baroclinic layer and about the centre of the Kelvin–Helmholtz vortex core (which is also a stagnation point); this symmetry results from the choice of the initial two-dimensional perturbation and from the symmetry conservation property of the Navier–Stokes equations. In the inner boundaries of the Kelvin–Helmholtz vortex two thin layers of vorticity of opposite (negative) sign to the vorticity of the baroclinic layer have developed. Thus, they form just below (or above, by symmetry) the part of the baroclinic layer that surrounds the Kelvin–Helmholtz vortex. Figure 20(j) shows that these negative vorticity layers are generated by strong streamwise density gradients, and indirectly result from convective activity in the vortex core. Each negative vorticity layer, together with the adjoining

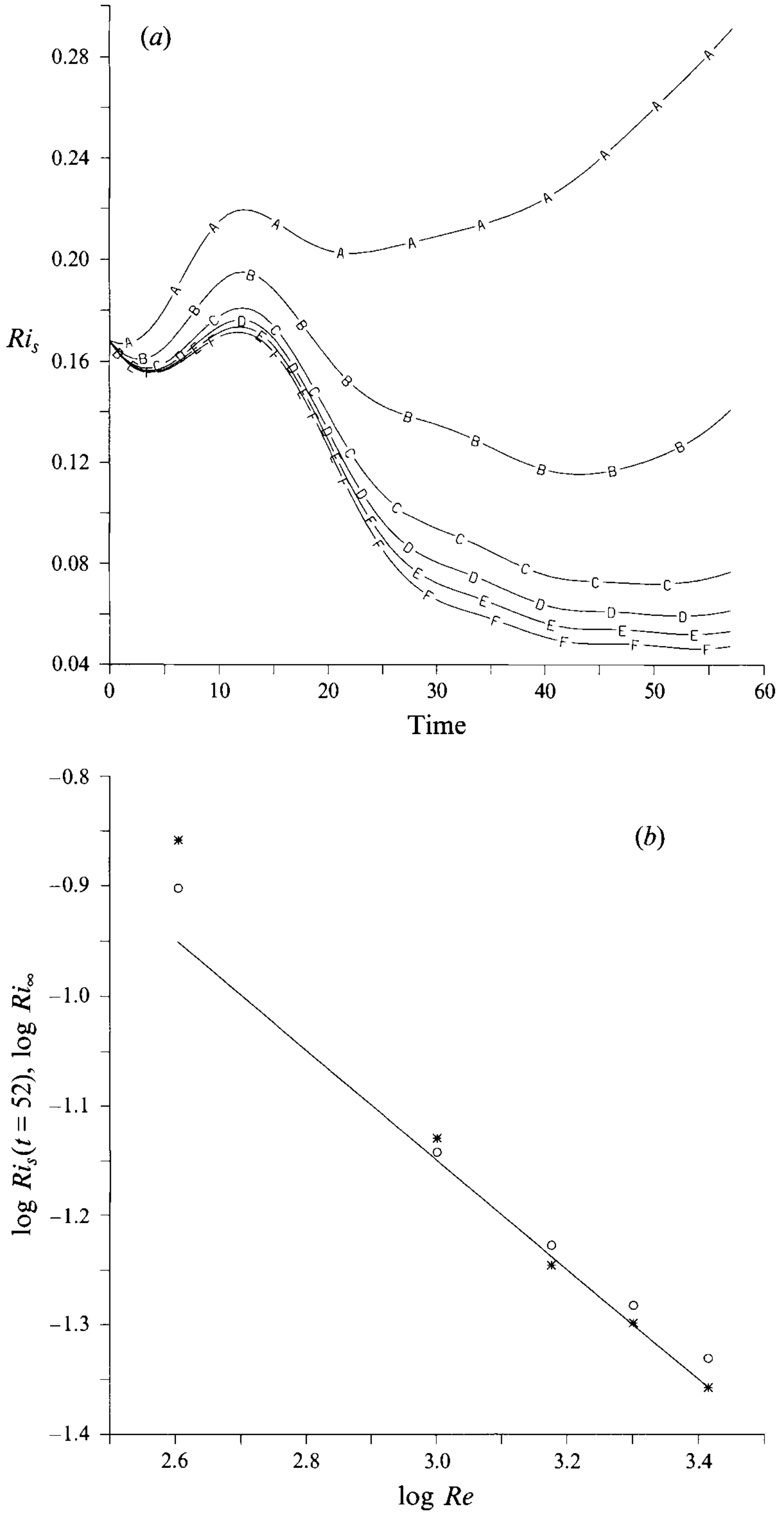

FIGURE 18. Richardson number at the stagnation point of the layer, Ri_s, defined by (3.1). (*a*) Versus time: A, $Re = 140$; B, $Re = 400$; C, $Re = 1000$; D, $Re = 1500$; E, $Re = 2000$; F, $Re = 2600$. (Runs 2–7.) (*b*) Versus Reynolds number, for $Re \geqslant 400$: ○, values computed numerically at $t = 52$; *, theoretical values Ri_∞ given by (3.9) at the same time. A log-log scale base 10 is used. The slope of the straight line is $-\frac{1}{2}$.

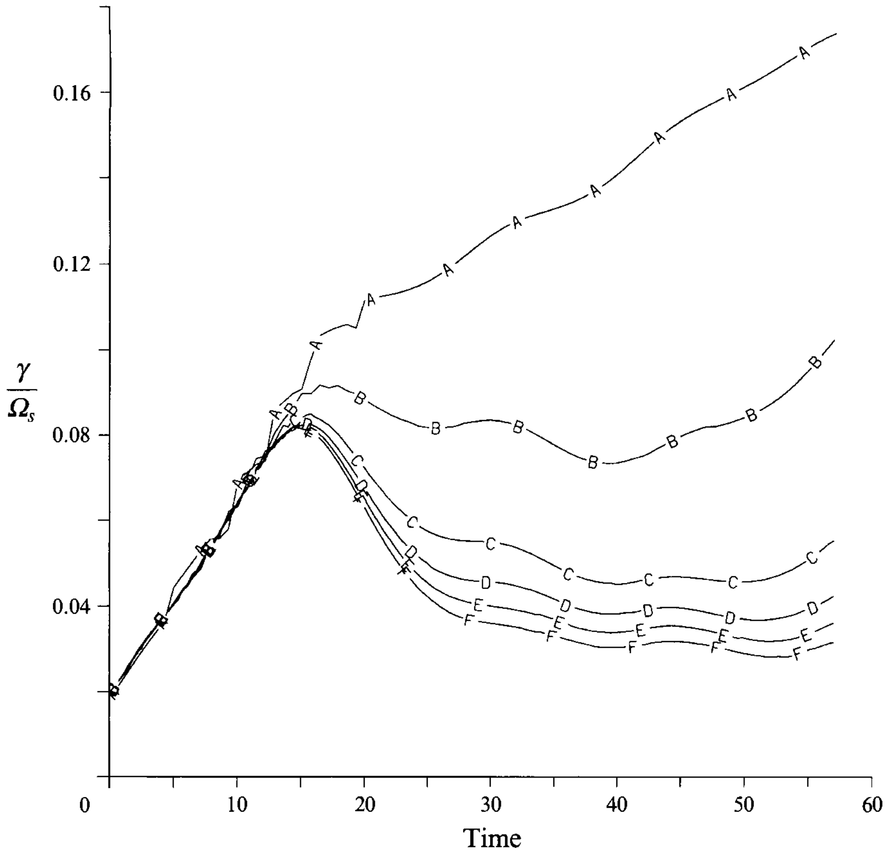

FIGURE 19. Temporal evolution of the strain rate γ over the vorticity at the stagnation point of the layer Ω_s: A, $Re = 140$; B, $Re = 400$; C, $Re = 1000$; D, $Re = 1500$; E, $Re = 2000$; F, $Re = 2600$. (Runs 2–7.)

baroclinic layer of positive vorticity, creates a jet flow. The earlier stage of the secondary instability growth is visible in figures 20(*b*, *c*). As noted above, this instability does not develop at the stagnation point of the baroclinic layer. Rather, it is this jet configuration that becomes unstable. Indeed, we have observed that the production of negative vorticity in the vortex core is rapidly followed by the growth of the secondary instability; moreover, this instability does not develop if the negative vorticity is too low compared to the positive one. However, this jet configuration is embedded in a complex and non-stationary flow, which does not facilitate a quantitative study of the instability. In the remainder of the paper, this secondary instability will be referred to as the 'near-core' instability.

The near-core instability amplifies while moving along the baroclinic layer. The velocity at which this instability moves can be estimated from visualizations of the vorticity field: a value equal to ≈ 0.85 is found, which lies in between the velocity of the baroclinic layer at the inner ($= 0.65$) and outer boundary ($= 1.3$). This suggests that the near-core instability is advected by the local velocity of the flow. Figures 20(*d*–*f*) show that the part of the baroclinic layer surrounding the Kelvin–Helmholtz vortex is next strongly bent out of shape: the growth of the moving secondary instability has indeed led to the formation of pairs of counter-rotating vortices, one in each layer of vorticity, which together induce a velocity that pushes the fluid towards the irrotational

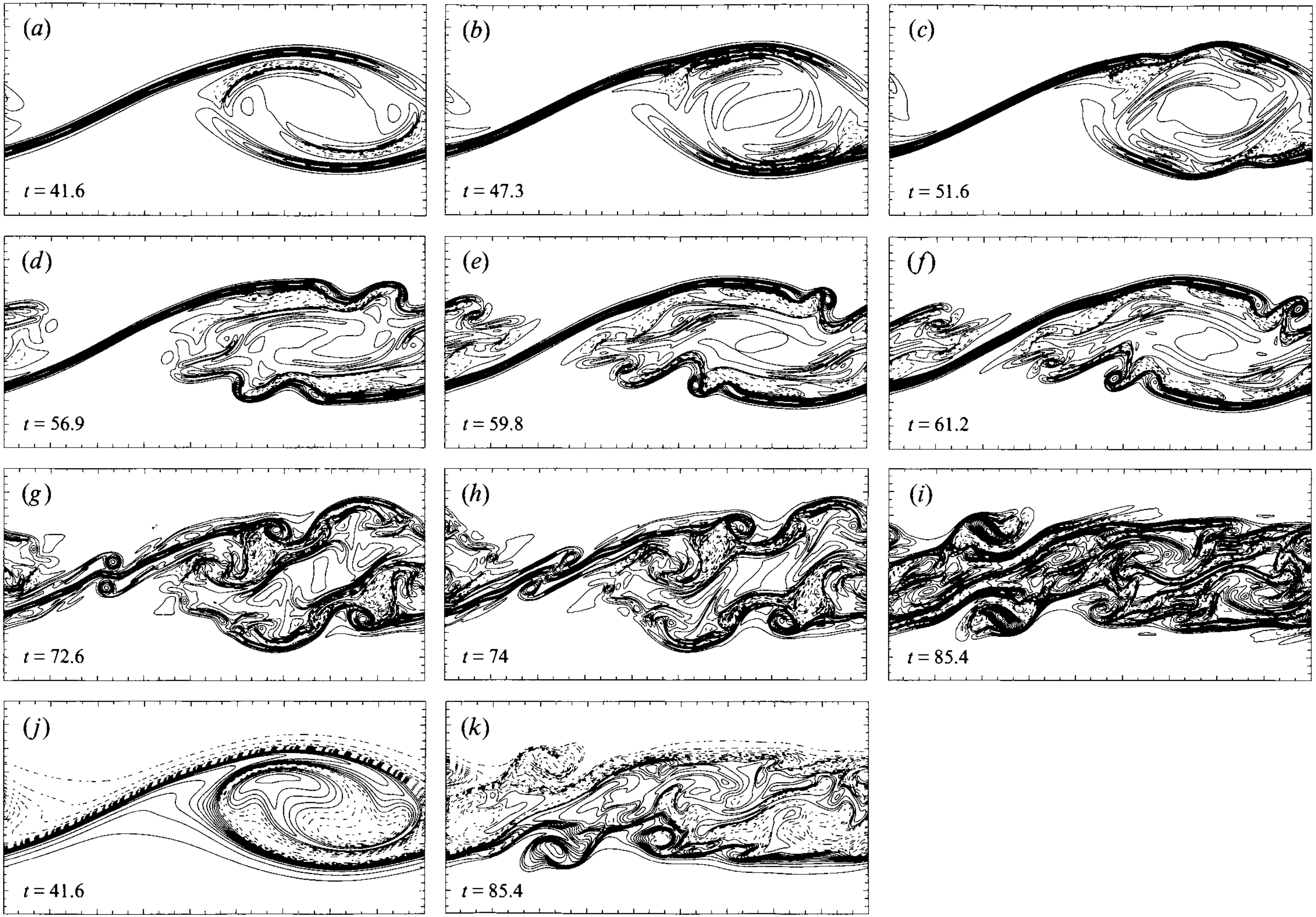

FIGURE 20. Development of secondary instabilities in a $Re = 2000$ shear layer (run 6). Only half of the numerical domain about the centreline is shown along the vertical. Contours of constant vorticity: (*a*) $\Omega_{max} = 4.8$; (*b*) $\Omega_{max} = 5.3$; (*c*, *d*) $\Omega_{max} = 5.5$; (*e*) $\Omega_{max} = 5.3$; (*f*) $\Omega_{max} = 5.2$; (*g*, *h*) $\Omega_{max} = 4$; (*i*) $\Omega_{max} = 3.6$. $d = 0.4$ except for (*i*) where $d = 0.3$. (*j*, *k*) Contours of constant density corresponding to (*a*) and (*i*) respectively; $d = 0.1$.

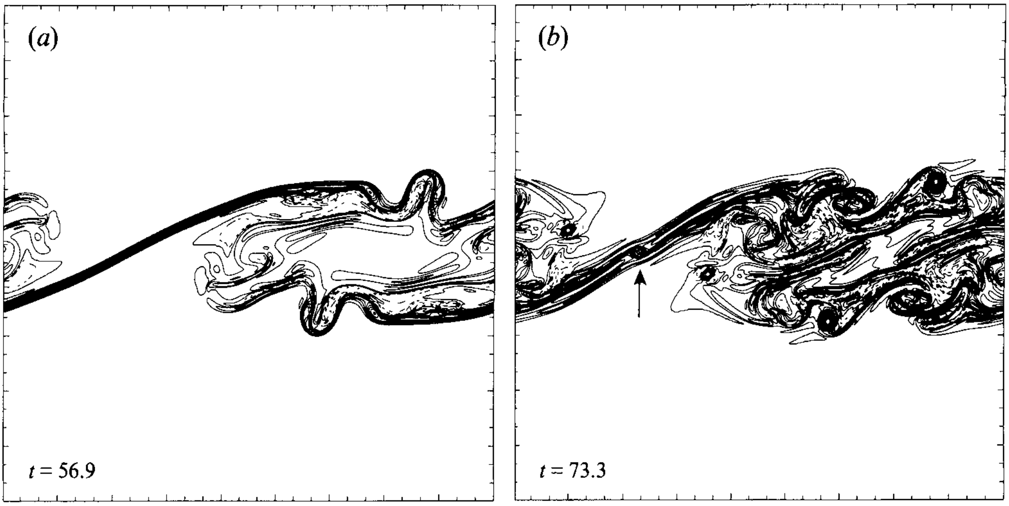

FIGURE 21. Development of secondary instabilities in a $Re = 2600$ shear layer (run 7). Contours of constant vorticity: (a) $\Omega_{max} = 6$; (b) $\Omega_{max} = 4.5$. $d = 0.5$. The arrow points towards a secondary Kelvin–Helmholtz vortex, which develops at the stagnation point of the baroclinic layer.

region of the shear flow. This distortion of the baroclinic layer is more striking when $Re = 2600$ (figure 21*a*), very likely because the absolute value of both positive and negative vorticity is higher then. The flow around the stagnation point of the layer becomes progressively modified by the approaching growing instability. Figure 20(*g*) shows that, in particular, two secondary vortices distort the vorticity layer there, eventually aligning it with the horizontal. This induces a strong perturbation in the baroclinic layer which becomes unstable a second time, now at the stagnation point (figure 20*h*). This secondary instability is of the Kelvin–Helmholtz type. When $Re = 2600$, a secondary Kelvin–Helmholtz instability develops at the stagnation point as well, in a strongly inclined baroclinic layer, once the near-core instability has moved into this region of the flow (figure 21*b*). This shows that the configuration of the two symmetric vortices near the stagnation point displayed in figure 29(*g*, *h*) was a very particular one. The flow next consists of thin quasi-horizontal layers and small-scale vortices, of both signs of vorticity, which give it a turbulent character (figure 20*i*). Note that the large-scale Kelvin–Helmholtz vortex has disappeared.

If the shear layer were unstratified, its mean thickness would grow linearly in time (e.g. Winant & Browand 1974). In the present case of a stably stratified shear layer, figures 20(*i*, *k*) show that this thickness reaches a constant limit. This behaviour has already been found and quantified by experimentalists. Thorpe (1973) defined a Richardson number, Ri_{max}, based upon the maximum mean thickness of the region of small-scale structures in the density field. This maximum thickness, h_{max}, was measured from photographs of the experiments. In Koop & Browand (1979), this maximum thickness is empirically related to the density integral scale

$$\theta_\rho = \frac{1}{\Delta\rho^2}\int_{-\infty}^{\infty} (\rho_B - \bar{\rho}(z))(\bar{\rho}(z) - \rho_T)\,\mathrm{d}z \tag{4.1}$$

by $h_{max} = 5\theta_\rho$. Here ρ_B and ρ_T are the values of the density at the lower and upper boundaries respectively. The computation of θ_ρ for run 6 shows that θ_ρ reaches a constant value equal to ≈ 0.90 from $t \approx 45$. With our notation, Ri_{max} is defined by

$$Ri_{max} = Jh_{max}/(2\delta_i) \tag{4.2}$$

which yields in the present case: $Ri_{max} = 0.37$. This latter value is in good agreement with Thorpe's study (for $R_I = 0.14$ again, see §3.1), whose experimental conditions were very close to those of our numerical simulations. This underlines the validity of our two-dimensional approach for this statistical property of the shear layer. By contrast, Koop & Browand found a much lower value for Ri_{max}, equal to 0.14. As already noted in §2.1, the mechanisms of instability at a high value of J in Koop & Browand's experiments are very different from those leading to a Kelvin–Helmholtz instability, the initial flow conditions leading instead to interfacial wave breaking.

Finally, we note that half the maximum thickness h_{max}, equal to 2.25, is very close to the maximum height reached by the Kelvin–Helmholtz vortex, equal to 2.15 in units of δ_i, that we computed in §3.1.

4.2. *Analogy with three-dimensional turbulence*

It is the non-conservation of the local vorticity that makes possible the successive secondary instabilities displayed in figures 20 and 21, in permitting the existence of a baroclinic layer of higher vorticity than the maximum initial vorticity, as well as the generation of negative vorticity. This non-conservation of the local vorticity is also a fundamental feature of three-dimensional turbulent flows, even without body force. We now examine whether this fundamental analogy may give rise to analogous behaviour. For this purpose, the dissipation rate of the total energy is examined as a function of the Reynolds number for the series of calculations presented above (runs 2–7 in table 1).

The dissipation rate of the total energy is made up of two contributions, respectively corresponding to the dissipation rate of the kinetic energy and of the potential energy. In the following, the word 'energy', whether total, potential or kinetic, will refer to a quantity averaged over the numerical domain. For a stably stratified shear layer in the Boussinesq approximation, it is easy to show that the dissipation rate of the potential energy ϵ_{EP} only depends upon the density difference $\Delta\rho$ between the upper and lower horizontal boundaries (assuming that there is no mass flux across these boundaries) and is thus constant in time. (This behaviour is discussed in Lombard, Stretch & Riley 1990.) The temporal evolution of the total energy can then be written as

$$\frac{\mathrm{d}E}{\mathrm{d}t} = -\frac{1}{Re}(Z + Re\,\epsilon_{EP}) \quad \text{with} \quad Re\,\epsilon_{EP} = -\frac{1}{L_z}\frac{J}{Pr}\Delta\rho. \tag{4.3}$$

Z is the enstrophy averaged over the numerical domain, defined by (2.9), and L_z is defined in (2.6). Note that ϵ_{EP} is negative in the present case of a shear layer, $\Delta\rho$ being positive. The constant value of ϵ_{EP} yields that the dissipation rate of the total energy is equal to Z^*/Re, where

$$Z^* = Z + Re\,\epsilon_{EP} \tag{4.4}$$

is simply the usual enstrophy with an additive constant. This additive constant is the same for all the calculations presented here.

Z^* is plotted in figure 22(*a*). Whatever the initial value of the Reynolds number (except possibly for $Re = 1000$), Z^* exhibits a first maximum at $t = 47$; this is close to the time at which the vorticity layer reaches an equilibrium state, as predicted by the model of Corcos & Sherman (1976) and checked in §3.3. The maximum vorticity of the flow is reached in the baroclinic layer up to this time (see figure 15*a*) and it is thus this part of the flow that controls the evolution of the total enstrophy. Z^* continues to increase for $Re \geqslant 1500$, when secondary instabilities develop in the baroclinic layer. A second maximum is then reached, at a time quasi-independent of the Reynolds number, equal to ≈ 64. The value of this second maximum is strongly dependent on

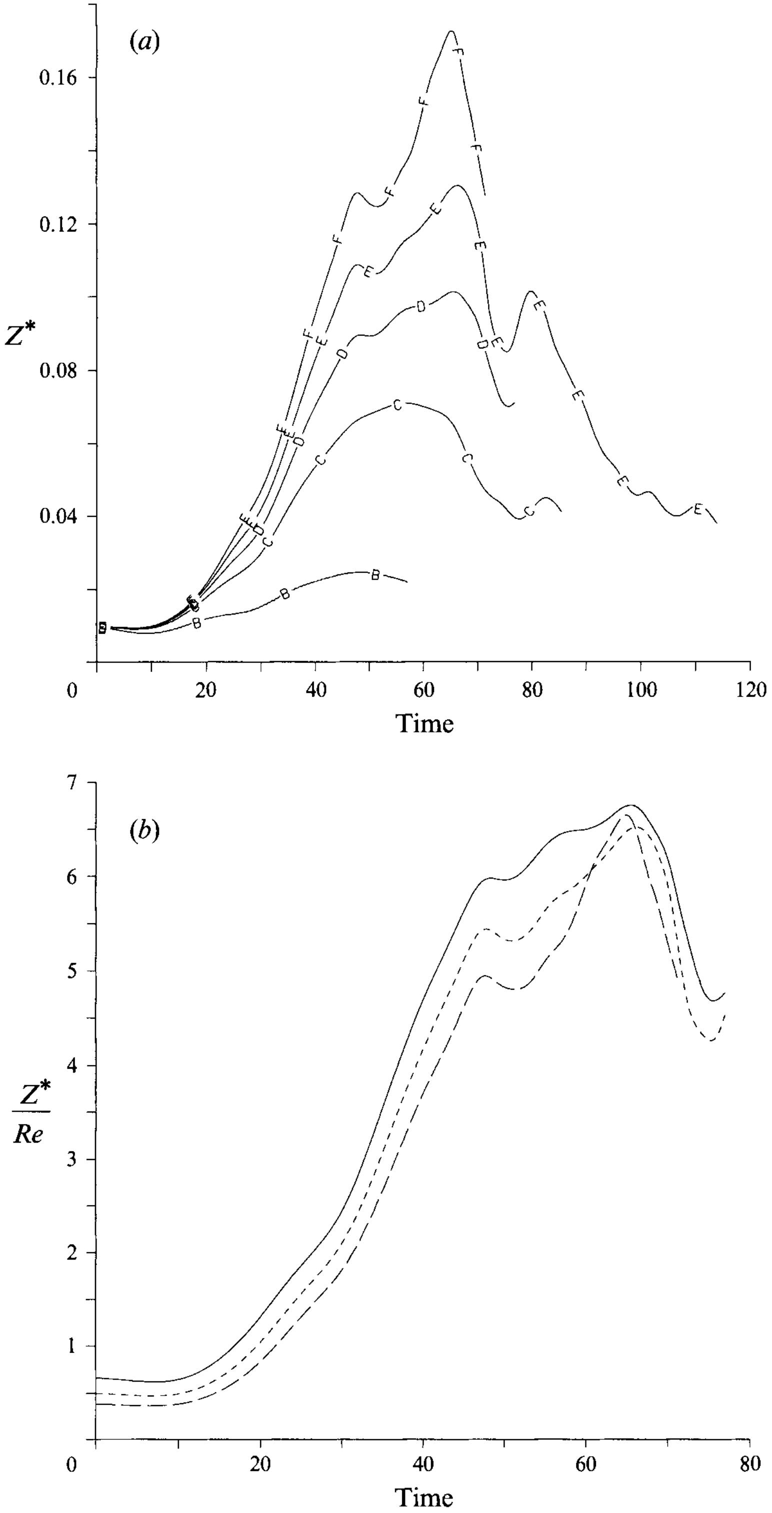

FIGURE 22. (*a*) Z^* defined by (4.4) versus time: B, $Re = 400$; C, $Re = 1000$; D, $Re = 1500$; E, $Re = 2000$; F, $Re = 2600$. (Runs 3–7.) (*b*) Z^*/Re, dissipation rate of the total energy, versus time for $Re \geqslant 1500$: ——, $Re = 1500$; ----, $Re = 2000$; — — —, $Re = 2600$. (Runs 5–7.)

the Reynolds number however and it is thus of interest to examine the behaviour of Z^*/Re for $Re \geqslant 1500$. This quantity is plotted in figure 22(*b*). The second maximum of Z^*/Re, reached at a time when the flow has become turbulent through secondary instabilities, seems to tend towards a constant limit as the Reynolds number increases. Such behaviour is analogous to that found for instance by Brachet (1990) for the three-dimensional unstratified Taylor–Green vortex. This suggests that the dissipation rate of the total energy becomes independent of the viscosity in the limit of zero viscosity; in other words, this dissipation rate is controlled by nonlinear effects in this limit (e.g. Lesieur 1990).

Note that this analogous behaviour between the viscous stably stratified shear layer modelled by the Boussinesq approximation and three-dimensional turbulence with finite viscosity parallels that used by, e.g., Pumir & Siggia (1992) between three-dimensional axisymmetric Euler equations with swirl and two-dimensional inviscid Boussinesq equations in their search for a possible singularity at a finite time of the three-dimensional Euler equations.

4.3. *Influence of a pairing on the growth of secondary instabilities*

It is clear that the late evolution (for $t \geqslant 70$) of the unstable flow displayed in figures 20(*g–i*) is strongly influenced by the periodic boundary conditions and by the symmetry of the flow. In order to examine the role of these numerical constraints upon the behaviour of the shear layer, a situation where two Kelvin–Helmholtz vortices can develop and pair will now be studied. As mentioned in §2.1, two different amplitudes of the subharmonic perturbation at $t = 0$ will be considered.

4.3.1. *Influence of a subharmonic perturbation of strong amplitude*

The calculation involving the subharmonic perturbation with the strongest amplitude is first described (run 12 in table 1). (We recall that the velocity amplitude of this subharmonic perturbation is 2.5 smaller than that of the fundamental perturbation.) The spatial distribution of the vorticity of the flow just before a secondary instability develops is displayed in figure 23(*a*). Note that the symmetry of the flow about its stagnation points is now broken, because of the presence of the subharmonic perturbation. The maximum of this perturbation is located at the centre of the right-hand vortex, while its minimum coincides with the centre of the left-hand one. Instabilities are thus promoted in the right-hand vortex: we observe indeed that the amplification of the secondary instability is much stronger for this vortex than for the left-hand one (figure 23*b*). This instability is the same as in figures 20 and 21: it develops near the unstably stratified regions of the vortex core and amplifies while moving along the baroclinic layer. It is thus a near-core instability. While amplifying, very small scales are generated, which quickly invade the whole area of the right-hand vortex (figure 23*d*). The filling of primary vortex structures by small-scale motions had already been noted by Thorpe (1971) in his experiments on a temporally growing shear layer. The baroclinic layer left behind the pairing vortices is stretched, thinned but reinforced by baroclinic effects: thus it becomes unstable a second time, now at its stagnation point (figure 23*c*, arrow 1). Figure 23(*d*) shows that this newly growing instability has the structure of a Kelvin–Helmholtz instability. As the secondary Kelvin–Helmholtz vortices are entrained at different velocities by the local shear, the vorticity layer between them is again stretched and reinforced by baroclinic effects, so that a new Kelvin–Helmholtz instability can develop there. Figure 23(*e*) thus displays Kelvin–Helmholtz vortices at different scales. If the initial Reynolds number were higher, the instability could proceed at smaller and smaller scales, thereby transferring

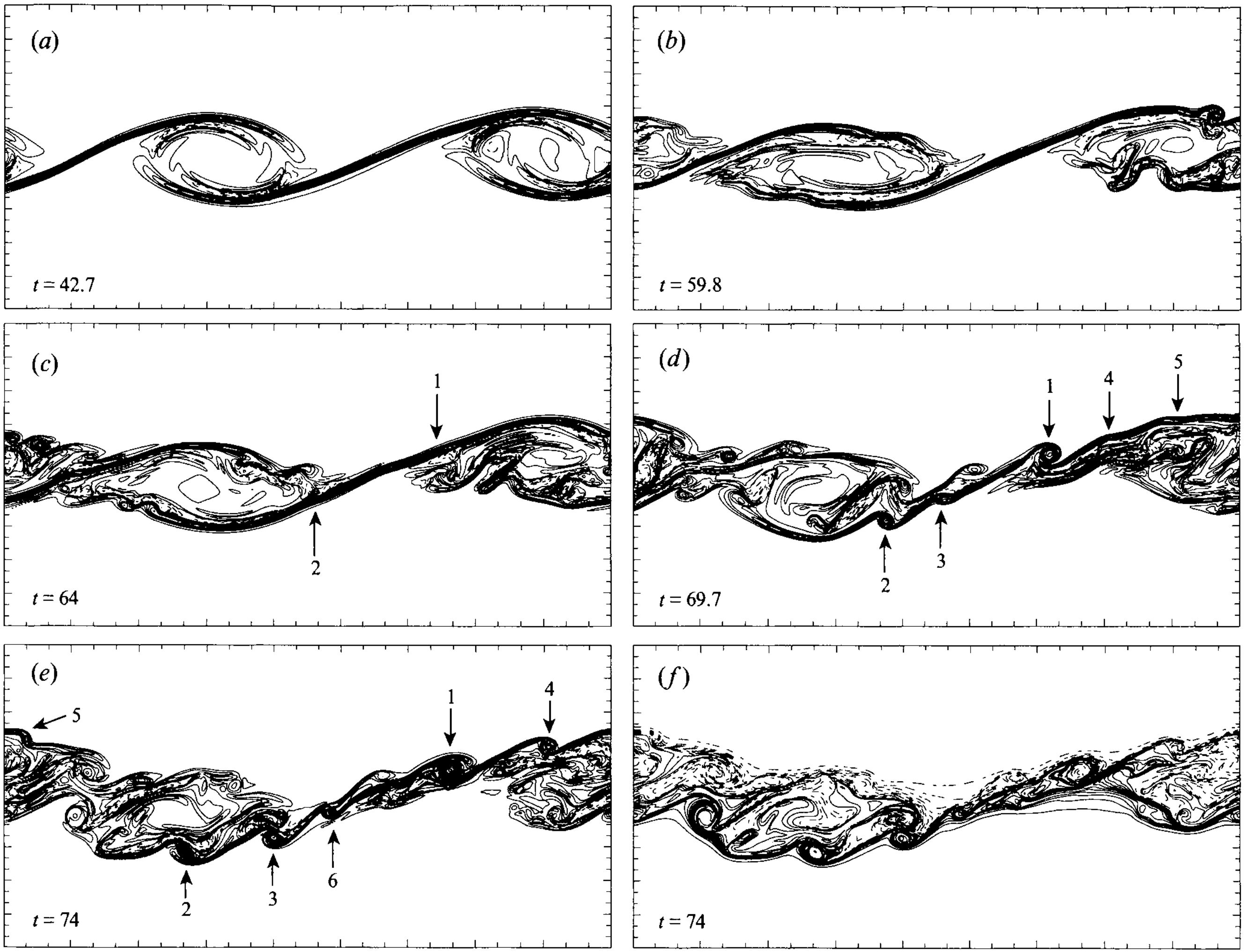

FIGURE 23. Development of secondary instabilities in a $Re = 2000$ shear layer with pairing (run 12). Contours of constant vorticity: (*a*) $\Omega_{max} = 4.8$; (*b*) $\Omega_{max} = 5$; (*c*) $\Omega_{max} = 5.2$; (*d*) $\Omega_{max} = 4.8$; (*e*) $\Omega_{max} = 4.4$. $d = 0.4$ except for (*b*) where $d = 0.5$. (*f*) Contours of constant density corresponding to (*e*); $d = 0.1$. The secondary Kelvin–Helmholtz vortices that develop in the baroclinic layer are visualized by arrows and numbered in order of appearance.

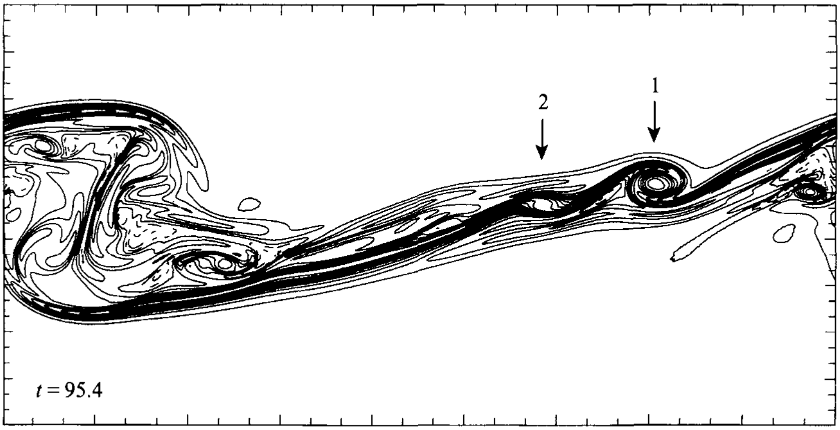

FIGURE 24. Development of a secondary Kelvin–Helmholtz instability in a $Re = 1000$ shear layer with pairing (run 10). Contours of constant vorticity are plotted at a given time, at which $\Omega_{max} = 2.2$. $d = 0.2$. The secondary Kelvin–Helmholtz vortices that develop in the baroclinic layer are visualized by arrows and numbered in order of appearance.

energy towards dissipative scales through a mechanism consisting in a succession of self-similar Kelvin–Helmholtz instabilities.

Figure 23 shows that pairing starts to occur, but at a slow rate. More precisely, the centre of the left-hand vortex remains at the same location in figure 23(*c*, *d*) (and the right-hand vortex hardly moves from one figure to the other), while secondary instabilities amplify: as noted by a referee, this suggests that the amplification of secondary instabilities may halt the development of the large-scale subharmonic instability, at least temporarily. Figure 23(*e*) shows indeed that the vortices have resumed their displacements, one towards the other, once the secondary instabilities have developed. This slowness of the large-scale subharmonic instability contrasts with the strong nonlinearity of the flow at small scales and illustrates the temporal decoupling between these scales of motion (buoyancy dominating over inertia at large scales, and vice versa at small scales).

At lower values of *Re*, between 400 and 1000, the flow dynamics exhibit a different behaviour. The near-core secondary instability does not develop (whether pairing occurs or not), possibly because the vorticity of the baroclinic layer and of the adjacent layer of negative vorticity are too weak to allow the development of this instability. More precisely, for this range of Reynolds numbers, the flow with one Kelvin–Helmholtz vortex is found to be always stable. By contrast, when two primary Kelvin–Helmholtz vortices can develop and pair, secondary Kelvin–Helmholtz instabilities are able to grow upon the baroclinic layer. This latter result is illustrated with two calculations for Reynolds numbers equal to 1000 and 400 (runs 10 and 9 in table 1) through constant contours of their vorticity (figures 24 and 25). Figure 24 exhibits two noticeable features: a large-scale vortex structure resulting from pairing, and the presence of two secondary Kelvin–Helmholtz vortices that have already grown in the baroclinic layer left behind by the pairing vortices. Vorticity contours of the $Re = 400$ shear layer are plotted in figure 25 at two successive times. Pairing clearly occurs in figure 25(*a*). In figure 25(*b*), a secondary Kelvin–Helmholtz instability develops in the baroclinic layer. As opposed to the pairing flows just described, the basic flow of this instability is the entire baroclinic layer (and not only its centre part): the rather large molecular viscosity may be responsible for this, in allowing for rapid diffusion of vorticity across the layer. Consequently, this instability is of large

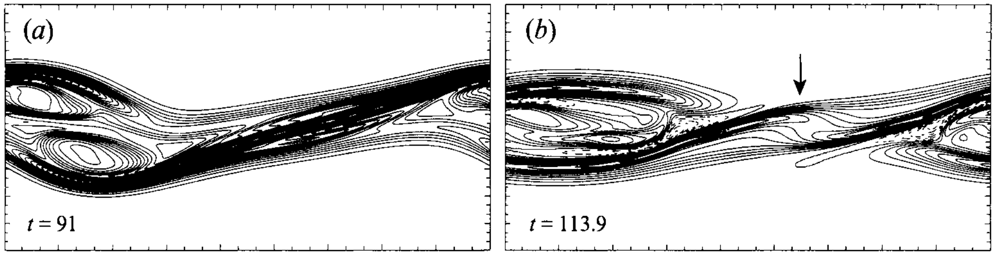

FIGURE 25. Development of a secondary Kelvin–Helmholtz instability in a $Re = 400$ shear layer with pairing (run 9). Contours of constant vorticity: (*a*) $\Omega_{max} = 1.36$; $d = 0.08$; (*b*) $\Omega_{max} = 1.3$; $d = 0.1$. The secondary Kelvin–Helmholtz instability that develops in the baroclinic layer is visualized by an arrow.

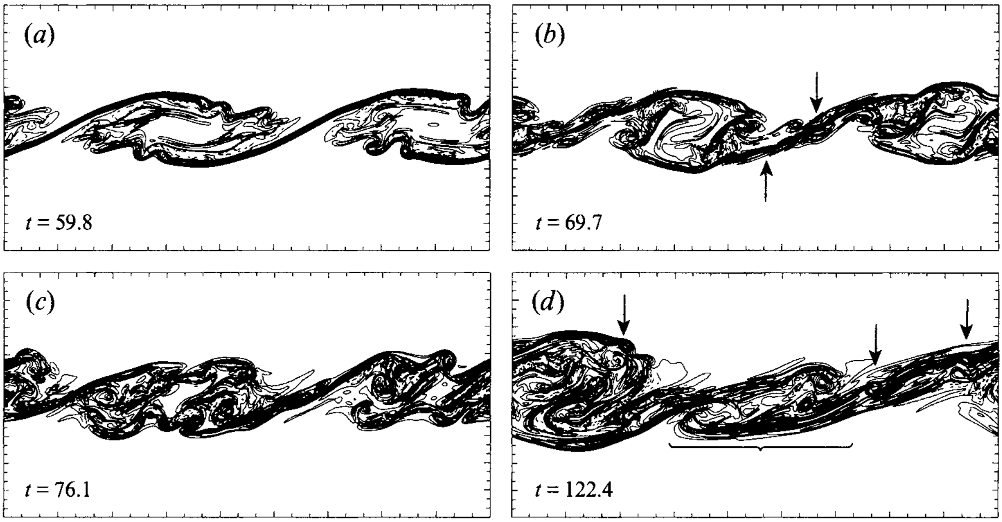

FIGURE 26. Development of secondary instabilities in a $Re = 2000$ shear layer with pairing (run 14). Contours of constant vorticity: (*a*) $\Omega_{max} = 5$; $d = 0.5$; (*b*) $\Omega_{max} = 4.5$; $d = 0.4$; (*c*) $\Omega_{max} = 4$; $d = 0.5$; (*d*) $\Omega_{max} = 3.5$; $d = 0.25$. The bracket and the arrows locate some secondary Kelvin–Helmholtz vortices.

wavelength, λ, because the half-thickness of the baroclinic layer, δ, is much larger than in previous calculations and $\lambda \approx 14\delta$, according to linear stability theory. The large-scale vorticity structures that form in this flow contrast with the very small scales displayed in figure 23 for the $Re = 2000$ counterpart flow.

4.3.2. *Influence of a subharmonic perturbation of weaker amplitude*

The calculations with $Re = 400$ and 2000 presented above have been carried out again with a velocity amplitude of the initial subharmonic perturbation equal to 1/10 of that of the fundamental mode (runs 13 and 14 in table 1). The main features of these calculations are described now. Pairing occurs, but very late in time, and the evolution of each flow does not change markedly compared to the situation described above where these flows were forced for pairing.

Constant contours of the vorticity when $Re = 2000$ are displayed in figure 26. Figure 26(*a*), plotted at the same time as figure 23(*b*), clearly shows the development of the near-core instability, which now affects both Kelvin–Helmholtz vortices: the promoting effect (on the right-hand vortex) and attenuating effect (on the left-hand

Re No. primary KH vortices	$\leqslant 400$	$400 \rightarrow 1000$	1500	$\geqslant 2000$
1 KH vortex	—	—	Second. NC instab.	Second. NC and KH instab.
2 KH pairing vortices	—	Second. KH instab.	Second. NC and KH instab.	Second. NC and KH instab.

TABLE 2. Growth of secondary instabilities in the baroclinic layer (KH: Kelvin-Helmholtz, NC: near-core), as a function of the initial Reynolds number and the number of primary Kelvin–Helmholtz vortices developing in the flow. Two different amplitudes of the subharmonic perturbation have been used (see §2.1) except for $Re = 1000$ and 1500, where the flow was only forced for pairing. For $Re = 400$, the secondary Kelvin–Helmholtz instability amplifies very weakly when the subharmonic perturbation has the lowest amplitude. —: No secondary instability.

vortex) of the subharmonic perturbation upon this secondary instability are less different in the present situation because of the lower initial amplitude of this perturbation. The near-core instabilities next amplify and move towards the stagnation point regions of the baroclinic layers. This triggers secondary Kelvin–Helmholtz instabilities in the right-hand baroclinic layer, as shown in figure 26(*b*) (a more complex situation sets in in the left-hand layer). Comparison with figure 23(*d*), plotted at the same time, shows that secondary instabilities have already amplified in the case of a stronger subharmonic perturbation. The earlier occurrence of pairing is responsible for this earlier unstable behaviour, as argued in §4.5. However the occurrence of pairing at a slower rate in the present case simply delays the development of secondary instabilities: figure 26(*c*) thus shows that both near-core and secondary Kelvin–Helmholtz instabilities amplify upon the baroclinic layers. Moreover, the growth of these secondary instabilities seems to temporarily halt the pairing process, as already noted for the forced case: the centres of the large-scale Kelvin–Helmholtz vortices have indeed remained at the same location, compared to figure 26(*b*). The evolution of the flow when we stopped the numerical simulation is displayed in figure 26(*d*): pairing clearly occurs. A hierarchy of instabilities is visible in this figure. Besides pairing, a large-scale secondary Kelvin–Helmholtz instability (visible in the middle of the figure and located by a bracket) has grown upon the whole baroclinic layer and is collapsing at the time the figure is plotted. Two small-scale secondary Kelvin–Helmholtz instabilities (located by arrows) are growing in the centre part of the baroclinic layer. Another small-scale secondary Kelvin–Helmholtz vortex is visible in the baroclinic layer surrounding the pairing vortices, having been advected there. This strongly unstable character of the flow thus induces a very complex behaviour. It seems, at this stage, that only a statistical description would provide quantitative and deeper insight into the dynamics of the flow.

For the $Re = 400$ calculation (not shown) pairing occurs as well, at a later time than in the counterpart flow forced for pairing: the stage of the flow displayed in figure 25(*a*) now occurs at $t \approx 120$. A secondary Kelvin–Helmholtz instability also develops in the baroclinic layer, while pairing is occurring; but, very likely because this instability grows late in time in a strongly stratified and rather viscous flow, it hardly amplifies.

The occurrence of a secondary near-core and/or Kelvin–Helmholtz instability in the baroclinic layer is summarized in table 2, depending upon the value of the initial Reynolds number and whether pairing is allowed to occur in the flow.

4.4. *An empirical criterion for the development of secondary Kelvin–Helmholtz instabilities*

In figure 23(*c*), the secondary Kelvin–Helmholtz instability develops at the stagnation point of the right-hand baroclinic layer from $t \approx 62$, that is at a time at which the outer velocity field acting upon the layer may still be modelled by a pure strain field. In order to get an idea of the threshold values for both γ/Ω_s and Ri_s below which a secondary Kelvin–Helmholtz instability develops (see §3.4), we have computed γ and γ/Ω_s for the calculation displayed in this figure. We assume then that the development of the near-core instability only provides the necessary perturbation to trigger the secondary Kelvin–Helmholtz instability, this perturbation being of small enough amplitude to preserve the structure of the outer strain field acting upon the layer.

The temporal behaviour of γ is displayed in figure 27(*a*) and compared to its evolution for the $Re \geqslant 1500$ calculations with one Kelvin–Helmholtz vortex with already plotted in figure 10. Notice that γ appears to be remarkably Reynolds-number independent for these three latter calculations. All curves in figure 27(*a*) exhibit the same initial growth rate and reach a maximum value at the same time ($t \approx 20$): the flow dynamics are driven by the growth of the fundamental perturbation up to this time (see figure 5). However, this maximum value is lower for the pairing calculation. Most interestingly, for this latter calculation γ next smoothly decreases and eventually attains half the value that it has in the non-pairing calculations. A physical argument to account for this behaviour, related to the concurrent growth of the subharmonic instability, will be provided in the next section.

The temporal behaviour of Ω_s for the pairing calculation is analogous to that of its non-pairing counterpart flow (run 6, plotted in figure 15*a*) up to $t \approx 30$, and increases slightly less from this time on (being at most 5% smaller); Ω_s next reaches an asymptotic limit from $t \approx 50$.

It follows that the ratio γ/Ω_s for the pairing calculation always has the smallest value as time evolves. This appears clearly in figure 27(*b*), where γ is now plotted relative to Ω_s. Figure 27(*b*) shows that γ/Ω_s for the pairing calculation reaches a minimum just before the secondary Kelvin–Helmholtz instability becomes visible, at $t \approx 57$ (see figure 23*c*). This minimum value is equal to 0.0185. At the same time, the Richardson number of the stagnation point of the layer is equal to 0.04. These two values, $\gamma/\Omega_s = 0.0185$ and $Ri_s = 0.04$, may provide thresholds for the development of the secondary Kelvin–Helmholtz instability. They are very small, which is consistent with the theoretical analysis derived by Dritschel *et al.* (1991).

As found by those authors however, it is very likely that the threshold value for γ/Ω_s below which amplification occurs strongly depends upon the amplitude of the perturbation at the stagnation point. Although possibly small in the present case, this amplitude is not infinitesimal. A linear stability analysis of this problem, whose basic profiles may be assumed to be stationary and made up of the vorticity and density profiles (3.7) subjected to a pure strain field of constant strain rate, would very probably lead to an even smaller threshold for amplification. It would be desirable to conduct such a stability analysis to test this idea and estimate the validity of our empirical results.

4.5. *Discussion*

We have shown that an earlier near-core secondary instability (as we refer to it) grows for $Re \geqslant 1500$ in the baroclinic layer, apparently once a negative vorticity layer of magnitude comparable with that of the positive vorticity of the adjacent baroclinic layer has formed in the inner boundary of the primary Kelvin–Helmholtz vortex. This

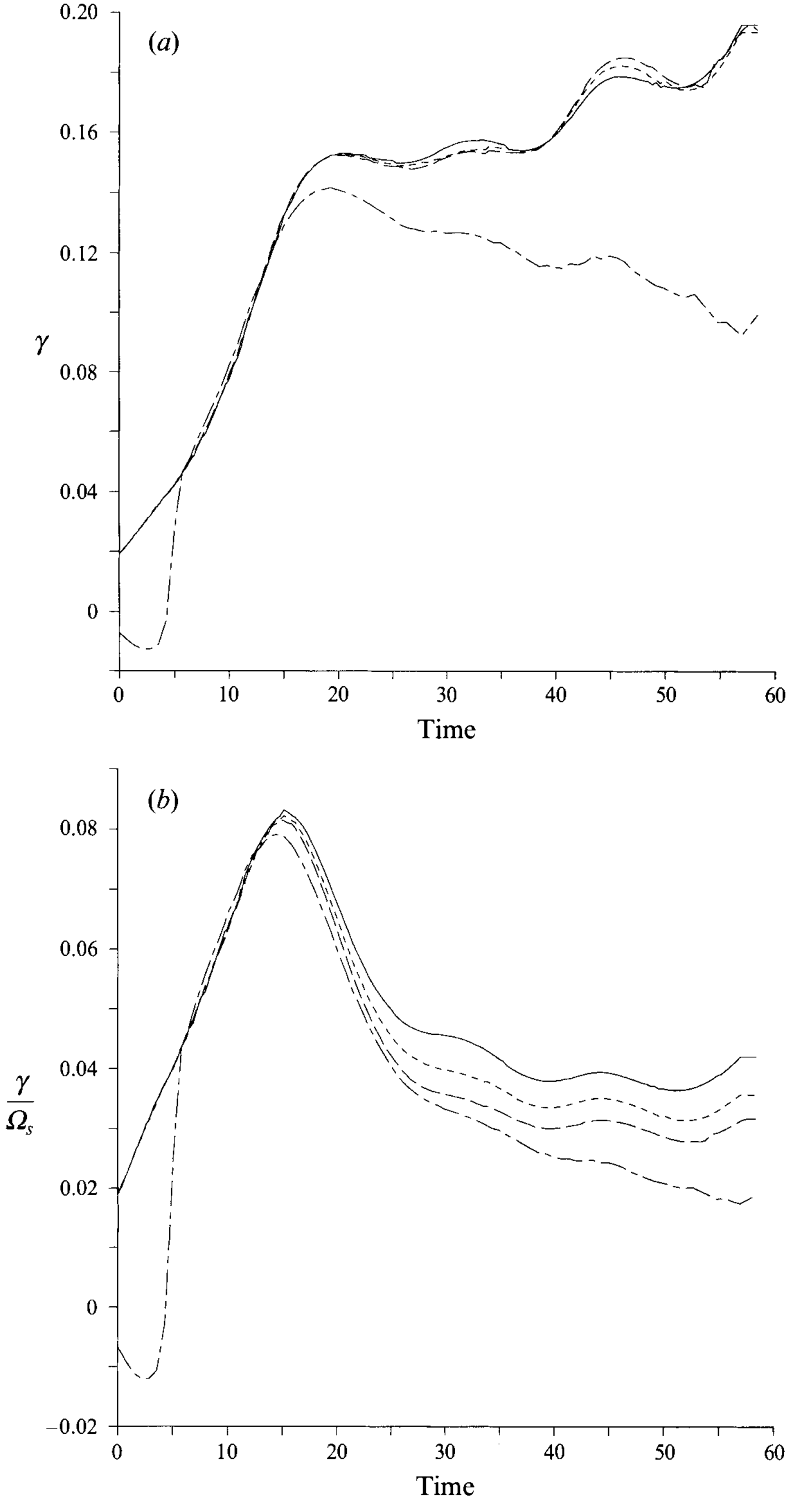

FIGURE 27. (*a*) Strain rate γ near the stagnation point of the baroclinic layer (see figure 10) versus time: ——, $Re = 1500$ (run 5); – – – –, $Re = 2000$ (run 6); — —, $Re = 2600$ (run 7); — - —, $Re = 2000$ (run 12). (*b*) Ratio of γ to the vorticity at the stagnation point of the layer, Ω_s, versus time for the same four runs.

negative vorticity is formed baroclinically when heavy (or light) fluid has completed a first revolution inside the primary Kelvin–Helmholtz vortex: such convective motion reinforces locally streamwise density gradients, in squeezing light fluid tongues between heavy fluid ones (see figure 20*j*). This convective motion essentially depends upon the development of the primary Kelvin–Helmholtz vortex, that is upon J: this is why, as shown in table 1, the near-core secondary instability develops at about the same time ($t_{NC} \approx 44$), quasi-independently of the Reynolds number.

These calculations have also shown that a necessary condition for a secondary Kelvin–Helmholtz instability to develop at the stagnation point of a baroclinic layer is that the stabilizing strain field acting in this region of the flow is suppressed, or at least significantly weakened. In all situations involving the growth of only one Kelvin–Helmholtz vortex, this condition is reached when the end part of the baroclinic layer, advected by the local shear, has invaded the stagnation point region. The outer velocity field acting upon the layer is thus no longer of the pure strain type; however this region soon becomes confined inside a complex flow: consequently, a strong enough perturbation has to be induced there to trigger the instability. This perturbation is provided by the near-core instability. This argument is supported by the fact that, when no near-core instability develops, the stagnation point of the baroclinic layer remains stable, even when its end part has reached the stagnation point region. This is the case for $Re \leqslant 1000$ (the length of the baroclinic layer may also come into play for $Re < 1000$, as discussed just below). As well, when $Re = 1500$, the amplification of the near-core instability is too weak to trigger an instability at the stagnation point and the baroclinic layer remains stable. A second necessary condition has to be fulfilled for the secondary Kelvin–Helmholtz instability to be able to grow, which is related to the length of the baroclinic layer compared to the wavelength of the perturbation. Since this wavelength is of order 14δ and δ is plotted in figure 12(*a*), it can be easily estimated. Figure 7 thus shows that this instability has enough space to grow upon the baroclinic layer for $Re \geqslant 1000$. It follows from this study of non-pairing flows that the secondary Kelvin–Helmholtz instability occurs rather late in the flow development, not before $t \approx 65$ according to table 1.

For a given value of Re, we have found that the baroclinic layer is much more unstable to secondary Kelvin–Helmholtz instability when pairing occurs in the flow. Indeed, such a secondary instability is found to develop for $Re \geqslant 400$ when the flow is forced for pairing, for $Re \geqslant 1000$ (very likely) when the kinetic energy of the subharmonic mode relative to that of the fundamental mode is divided by ≈ 16 compared to the forced case, and for $Re \geqslant 2000$ when no pairing occurs. The occurrence of pairing always arises late in time because we are dealing with strongly stratified flows, so that the end part of the baroclinic layer has already been advected into the stagnation point region at that time (except for run 12, as discussed below). But, as opposed to the non-pairing flows described above, pairing relaxes the strong constraint of the confinement of the layer (see figures 24 and 25), which promotes the secondary instability growth. Also, the length of the layer increases while pairing is occurring, so that this layer soon becomes able to sustain the wavelength of the secondary instability, even at low Reynolds number.

For run 12, involving a strong-amplitude subharmonic perturbation and a high initial Reynolds number ($Re = 2000$), pairing occurs faster than for any other calculation involving pairing. We also observe that the secondary Kelvin–Helmholtz instability develops early, and that, at that time the end part of the baroclinic layer has not yet invaded its stagnation point region. Thus, as we assumed in the previous section, the secondary Kelvin–Helmholtz instability develops upon a baroclinic layer still subjected to a pure strain field. The strain rate has however been weakened (see figure 27), which permits the growth of the instability. To understand this, we have to relate the occurrence of pairing to the smaller value of the strain rate. For this purpose, we need to recall the definition of the strain rate induced by the primary Kelvin–Helmholtz vortices at the stagnation point of the baroclinic layer located in between them. From the Biot–Savart law, γ is roughly proportional to the circulation of the vortices divided by the distance squared between each vortex (its centre, say) and the stagnation point. When the vortices move towards each other for pairing, their circulation decreases (or, at best, remains unchanged), while their distance from the stagnation point increases. It follows that γ decreases during this event. Arguments can also be provided for the vorticity at the stagnation point of the layer, Ω_s, to keep nearly the same asymptotic limit as in the non-pairing flow: though the angle of the baroclinic layer with the horizontal decreases when pairing is initiated, and so therefore does the baroclinic production of vorticity, the advection rate (equal to γ) of this vorticity also decreases, which leaves the velocity difference across the baroclinic layer about constant (see §3.1). Because the layer is stretched by the pairing process, its thickness (which should increase by (3.2)) remains about the same. It follows that the ratio γ/Ω_s decreases during pairing, which relaxes the strength of the outer strain field and permits the growth of the secondary Kelvin–Helmholtz instability.

This argument is not specific to pairing flows. For instance, in a natural (i.e. unforced) shear layer, the relative phase of the primary Kelvin–Helmholtz vortices is random along the streamwise direction. If two such vortices grow far enough apart, the baroclinic layer in between them becomes less constrained and a secondary instability may amplify. This can be checked easily by initializing a numerical simulation with a random perturbation (a white noise perturbation, for the stream function), instead of a deterministic perturbation, in a numerical domain of long enough streamwise extent (run 15 in table 1). Such a calculation is presented in figure 28, the streamwise extent here being equal to four fundamental wavelengths. For some realization of the white noise, only three Kelvin–Helmholtz vortices develop in the numerical domain (the relative phases of the wavenumbers, which are all initially present, being randomly distributed) (figure 28*a*). A secondary instability is observed in the longest baroclinic layer that forms in between the primary vortices (figure 28*b*).

This argument has also been illustrated numerically in Staquet (1994), to allow a more quantitative study. In that paper, the length of the baroclinic layer is progressively increased, in order to make the strain rate γ, and thus the ratio γ/Ω_s, decrease. Only when γ/Ω_s goes below the value of ≈ 0.02 (with $Ri_s \approx 0.07$) does a secondary Kelvin–Helmholtz instability develop at the stagnation point of the layer. This value is consistent with the threshold value found in the present study (the Richardson numbers at the stagnation point having closed values). It is interesting to mention that, as the length of the baroclinic layer is increased, Ri_s remains about the same. Thus, in this study, the stability of the layer is clearly controlled by the parameter γ/Ω_s.

It is reasonable to assume that the threshold value for γ/Ω_s below which a secondary instability may develop does not depend upon viscous effects: this secondary instability is of the Kelvin–Helmholtz type, which is an inviscid instability. The viscosity comes into play only indirectly, in imposing a constant thickness on the baroclinic layer. We also assume that the threshold value found for γ/Ω_s does not depend upon the amplitude of the perturbation leading to the instability, that is that this threshold value was computed during a linear regine. This threshold value has been obtained for a fixed value of Ω_s (as shown above) and for γ decreasing (through pairing). We shall now use this result to estimate the minimum initial Reynolds number (Re_{min}) that is necessary

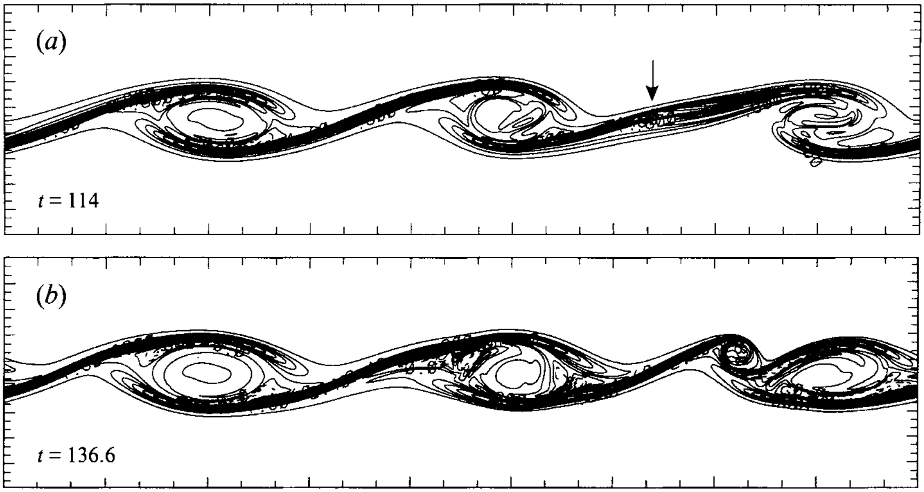

FIGURE 28. Run 15. Contours of constant vorticity. (a) $\Omega_{max} = 2.8$; the location where a secondary Kelvin–Helmholtz instability starts growing is indicated by an arrow. (b) $\Omega_{max} = 3.2$, $d = 0.2$.

for a secondary Kelvin–Helmholtz instability to develop upon the baroclinic layer of the flows with one Kelvin–Helmholtz vortex that we have studied. γ will now have a fixed value and it is Ω_s that will vary (through *Re*). The baroclinic layer is assumed to be subjected to a pure strain field, with only a small perturbation to trigger the instability. We use Corcos & Sherman's model in a predictive manner. The minimum Reynolds number that we seek is the one for which the vorticity satisfying the criterion $\gamma/\Omega_s = 0.0185$ is the maximum vorticity of the flow. The expression for this maximum vorticity is (3.8). Thus, on plugging $\gamma/\Omega_s = 0.0185$ into (3.8), one gets $Re_{min} \approx 5850$ (with $\gamma = 0.18$, $\theta = 27°$ and $\Delta\rho_L = 1.78$, from §3.3.2, which are all parameters independent of the Reynolds number). For this threshold Reynolds number, the instability would grow from $t \approx 52$ (see figure 15*a*) and this time should decrease for $Re > Re_{min}$. This earlier occurrence of a secondary Kelvin–Helmholtz instability is currently impossible to obtain in a direct numerical simulation but is very likely to occur in a strongly stratified geophysical flow.

Finally, note that, in all calculations of the present paper, the development of the secondary Kelvin–Helmholtz instability yields the formation of well identified vortices compared to the primary Kelvin–Helmholtz instability. This is attributable to the very small value of the Richardson number of the baroclinic layer.

4.6. *Comparison with theoretical predictions and numerical observation of secondary instabilities in a stably stratified shear flow*

4.6.1. *Theoretical predictions*

Klaassen & Peltier (1989) have analysed the stability of a primary Kelvin–Helmholtz vortex to two-dimensional perturbations. For flow parameters $Re = 300$, $J = 0.07$ and $Pr = 1$ they found an instability located at the stagnation point of the baroclinic layer, of the same periodicity as the Kelvin–Helmholtz wave. They suggested that this 'braid instability', as they refer to it, may correspond to a secondary Kelvin–Helmholtz instability. However, they noted several important differences between the two instabilities, among them being that the structure of the eigenfunction of the braid instability does not match that of the Kelvin–Helmholtz instability. Moreover, we noted in §4.5 that, because of the stabilizing action of the outer pure strain field, a secondary Kelvin–Helmholtz instability may be able to grow upon a baroclinic layer only for a very high value of the initial Reynolds number. For the flow parameters studied by Klaassen & Peltier, the minimum value of Re would be equal to 11000 (see Staquet 1994). These remarks suggest that the braid instability found by Klaassen & Peltier may not be of the Kelvin–Helmholtz type. We also notice that no secondary near-core instability was reported in their stability analysis. The low value of Re may again be responsible for this (no negative vorticity being visible in the inner boundaries of the primary Kelvin–Helmholtz vortex whose stability is investigated).

Maslowe (1972) has calculated the structure of the critical layer in a stratified shear flow for finite-amplitude neutral waves at high Reynolds number. The stationary Boussinesq equations are solved analytically (using the method of matched asymptotic expansions) in a frame of reference attached to the phase speed of the neutral wave. The solution found by Maslowe inside the largest closed streamline has a cat's eye structure, is inviscid and has a uniform density. Because buoyancy is present however, thin viscous and thermal layers need to be introduced at the boundaries of the cat's eye to remove discontinuities in velocity and temperature. Maslowe showed that the velocity field in these 'diffusive layers' is a shear and that the density profile there has an identical shape. Moreover, the Richardson number is much smaller than $\frac{1}{4}$ in the layers, even when this parameter exceeds this critical value everywhere in the remainder of the flow. A secondary instability is then expected to develop in these diffusive layers.

The structure of Maslowe's solution has striking similarities with our numerical results (e.g. figure 3*d*) and is located where the near-core instability amplifies in our calculations. However, Maslowe's theoretical study exhibits two important differences with our numerical two-dimensional calculations. First the analysis is stationary and, secondly, the density inside the cat's eye is uniform. This contradicts the interpretation for the origin of the near-core instability that we have proposed, which results from intense convective activity in the vortex core. (It should be noticed that, according to Haberman 1973 or Troitskaya 1991, Maslowe's calculations involve a simplification which may influence the critical layer dynamics; see also Maslowe 1986.)

4.6.2. *Comparison with a three-dimensional numerical simulation of a strongly stratified shear layer.*

The simulations of one Kelvin–Helmholtz vortex analysed in §3 involve a calculation at low Reynolds number, equal to 140 (run 2 in table 1). A three-dimensional flow having the same values of J and Re is described in Staquet (1991). A large-scale three-dimensional perturbation is superimposed at $t = 0$ upon the flow used to initialize the $Re = 140$ two-dimensional calculation. (Note that large-scale three-dimensional perturbations are observed to grow in the laboratory experiments of unforced stably stratified shear layers performed by Yoshida, Caulfield & Peltier 1994, which gives substance to our choice of the three-dimensional perturbation.) The purpose of the present section is to compare the evolution of the two- and three-dimensional flows.

The three-dimensional flow behaves totally differently than its two-dimensional counterpart: a secondary Kelvin–Helmholtz instability develops in a baroclinic layer of the flow, at $t \approx 65$, at a location where the spanwise vorticity reaches an absolute maximum (equal to 2.25). This maximum value is almost twice as big as for the two-dimensional flow (see figure 7*a*): both the baroclinic torque and vortex stretching are responsible for production of positive spanwise vorticity in the three-dimensional flow. Also, the thickness of the baroclinic layer appears to be half that in the two-dimensional situation. As a consequence, the local Richardson number of the baroclinic layer reaches a value as small as 0.03 when the secondary instability develops. This parameter becomes the only one that needs to be considered in this three-dimensional situation, since no two-dimensional pure strain field acts any longer upon the layer. As in two-dimensions, a well identified secondary Kelvin–Helmholtz vortex is able to grow. It should be pointed out that, in this low-Reynolds-number three-dimensional flow forced at the largest spanwise wavelength, no other clearly identified instability was detected.

5. Summary and conclusions

The purpose of the present study is to investigate numerically the occurrence of two-dimensional secondary instabilities in a baroclinic layer of a strongly stratified shear layer. To our knowledge, the occurrence of such instabilities has only been reported in geophysical flows (Gossard *et al.* 1970; Haury *et al.* 1979), in a few laboratory experiments (Delisi 1973 and personal communication 1994; Altman 1988; Atsavapranee 1995) and in one three-dimensional numerical simulation (Staquet 1991). A baroclinic layer is a thin inclined vorticity layer, whose vorticity is produced by the streamwise gradient of the local density field. The baroclinic layer forms in between the primary Kelvin–Helmholtz vortices at the location where the 'braid' develops in an unstratified shear layer. The formation of baroclinic layers is a fundamental aspect of the flow, as a manifestation of the property that the vorticity is no longer a Lagrangian invariant of the flow (in the inviscid case), as it would be if the density were uniform. This gives the stably stratified shear layer a totally different behaviour than its unstratified counterpart, with local increase of the vorticity beyond its maximum initial value and transfer of energy towards small scales, as in three-dimensional turbulence. This study is two-dimensional, with minimum Richardson number equal to 0.167 for all calculations.

The influence of the initial Reynolds number upon the dynamics and the structure of the baroclinic layer in the neighbourhood of its stagnation point is examined first in the light of the theoretical model proposed by Corcos & Sherman (1976). One of the predictions of the model is the existence of an equilibrium state for the baroclinic layer. Detailed comparison with the structure of the layer when this equilibrium state is reached are made, and remarkable agreement with the predictions of the model are found.

Almost up to the time when this equilibrium is reached, the baroclinic layer remains stable. Still, the Richardson number at its stagnation point (where this parameter becomes smallest) may become as low as 0.046. For such a value, linear stability analysis of a horizontal shear layer subjected to a parallel velocity field predicts instability. We argue that the outer strain field acting upon the baroclinic layer about its stagnation point is at the origin of this persistent stability, in contributing an additional stabilizing mechanism, besides the stable stratification. To quantify this additional stabilizing effect, we compute the strain rate γ relative to the vorticity Ω_s at the stagnation point of the baroclinic layer. We find that even a ratio γ/Ω_s as small as 0.027 is enough to prevent the growth of the instability. This is consistent with the findings of Dritschel *et al.* (1991), for the case of an unstratified strip of uniform vorticity in an inviscid fluid subjected to a pure constant strain field. The ratio found here is even smaller, the weak but non-zero value of the Richardson number of the layer ($= 0.046$) being very likely at the origin of this difference.

Two different secondary instabilities are eventually found to develop upon the baroclinic layer. For $Re \geqslant 1500$, a first instability appears just before the equilibrium state mentioned above has been reached. This instability does not develop at the stagnation point of the layer and is not of the Kelvin–Helmholtz type. It grows near the statically unstable region of the primary Kelvin–Helmholtz vortex. One necessary condition for this instability to grow seems to be the formation of a strong jet made by the baroclinic layer and an adjacent vorticity layer of opposite sign, created baroclinically by convective motions inside the primary Kelvin–Helmholtz vortex. It is this jet flow which would become unstable. This secondary 'near-core' instability, as we refer to it, amplifies while moving along the baroclinic layer towards the stagnation point region. Consequently, it perturbs the whole flow field and induces a turbulent behaviour. To our knowledge, this secondary instability has never been reported previously.

Another secondary instability, now of the Kelvin–Helmholtz type, is found to develop at the stagnation point of the baroclinic layer. According to the arguments given above, the outer strain field acting upon the layer there needs to be suppressed, or weakened enough, for this instability to be able to grow. When only one primary Kelvin–Helmholtz vortex develops in the flow (i.e. pairing is prohibited), this instability is found to occur for $Re \geqslant 2000$. Indeed, in moving toward the stagnation point region, the near-core instability does destroy the outer strain field, but, in doing so, also confines the layer to a complex flow. We argue that only when the perturbation induced by the near-core instability is strong enough can the secondary Kelvin–Helmholtz instability develop; this occurs for $Re \geqslant 2000$.

By contrast, when a subharmonic perturbation is added at $t = 0$, this secondary Kelvin–Helmholtz instability is found to grow for $Re \geqslant 400$, while pairing is occurring. Because this latter event occurs late in time, the stagnation point region of the layer has already been invaded by the rotational part of the flow at that time. But pairing both reduces the confinement of the layer and increases its length, so that an instability now can eventually grow upon the layer, even if rather thick. An interesting situation is encountered when the flow is forced for pairing at high initial Reynolds number ($Re = 2000$). In this case, pairing occurs much faster than in any other calculations. This permits the growth of the secondary instability upon a baroclinic layer still subjected to the strain field: indeed, in moving away from the stagnation point, the primary vortices induce a weaker strain field there, so that a secondary instability is able to develop before rotational flow has been advected by the local shear in this region of the layer. From this calculation, an empirical threshold value for γ/Ω_s below which the instability may develop is inferred. A threshold value as small as 0.0185 is obtained, with a local Richardson number equal to 0.04. The smallness of the former value is consistent with the theoretical findings of Dritschel *et al.* (1991). Hence, though this study is performed at a high value of J, it may help to understand why previous two-dimensional numerical studies of moderately stably stratified shear layers did not report the occurrence of any secondary instability: it is very likely that the initial Reynolds number was too low.

In the $Re = 2000$ pairing situation described above, vorticity is continuously regenerated baroclinically in the stretched baroclinic layer and we show that secondary Kelvin–Helmholtz instabilities successively occur there, at smaller and smaller scales. This suggests a mechanism of transfer of energy towards dissipative scales, through a 'cascade' of self-similar Kelvin–Helmholtz instabilities. Such a mechanism could contribute to mixing at small scales in geophysical flows, in agreement with Woods' (1969) conjectures. These successive secondary instabilities next destabilize the whole flow, as the newly formed secondary vortices are entrained by the local shear. The flow soon displays turbulent behaviour. At this stage, a statistical description would be required to gain a global and quantitative insight into the flow dynamics.

As noted above, the non-conservation of the vorticity following a fluid particle suggests that the flow may possess properties analogous to three-dimensional turbulence. We have found that the dissipation rate of the total energy exhibits a maximum value which does not depend upon *Re* when the flow has become turbulent through secondary instabilities (this is the case for $Re \geqslant 1500$). It follows that the dissipation rate of the total energy would be controlled by inertial effects in the limit of zero viscosity. This behaviour is analogous to that found numerically by Brachet (1990) in three-dimensional homogeneous isotropic turbulence.

This work raises many questions. For instance, how would the two-dimensional secondary instabilities revealed by our calculations behave and possibly compete with intrinsically three-dimensional instabilities? Schowalter *et al.* (1994) have clearly demonstrated experimentally the formation of a convective instability in the vortex core, which would be located close to the place where the secondary near-core instability develops. At a high stratification level, Klaassen & Peltier (1991) predicted that a 'dynamical' instability may develop in the neighbourhood of the Kelvin–Helmholtz vortex, more or less at the location where the near-core instability grows. (This prediction was obtained by studying the stability to three-dimensional perturbations of a shear layer with one Kelvin–Helmholtz vortex.) Moreover, both inertial and convective effects would be at the origin of this dynamical instability, just as for the near-core instability. The intrinsically three-dimensional character of the former instability, however, prohibits any further link with the latter. How our near-core instability would interact with these three-dimensional convective and dynamical instabilities, in a fully three-dimensional calculation, is an open question.

Also, how important is mixing induced by the occurrence of the near-core and Kelvin–Helmholtz secondary instabilities? How do vertical diffusion coefficients compare with estimates stemming from experimental or *in situ* measurements? This is a crucial question in oceanography (see e.g. Garrett 1993), which would need to be examined.

This work also raises more fundamental questions. First, the stability of a baroclinic layer subjected to an outer strain field should be addressed. It would allow an estimate of the validity of the approach used here to account for the stability of the baroclinic layer in the neighbourhood of the stagnation point, and derive precise threshold values for γ/Ω_s and the Richardson number of the layer below which instability occurs.

Also, our two-dimensional numerical simulations have suggested the existence of a cascade of secondary Kelvin–Helmholtz instabilities towards dissipative scales. What would this cascade lead to in the absence of viscosity? The limit flow behaviour, if found, would be of great interest if one remembers the analogy already used by e.g. Pumir & Siggia (1992) between the inviscid two-dimensional Boussinesq equations and the three-dimensional Euler equations with swirl.

This work benefitted from discussions with L. Armi, D. Dritschel, S. Maslowe, A. Pumir and J. J. Riley. Valuable comments were provided by J. Sommeria on a preliminary draft of this work. Computations have been performed on the Cray 2 of CCVR (Centre de Calcul Vectoriel pour la Recherche) and on the Cray C98 of CNRS. Part of the computation time has been allocated by the Scientific Committee of CCVR.

REFERENCES

ALTMAN, D. B. 1988 Critical layers in accelerating two-layer flows. *J. Fluid Mech.* **197**, 429–451.

ATSAVAPRANEE, P. 1995 The dynamics of a stratified mixing layer with cross shear. PhD thesis, University of California, San Diego.

BATCHELOR, G. K. 1967 *An Introduction to Fluid Dynamics*. Cambridge University Press.

BAYLY, B. J., ORSZAG, S. A. & HERBERT, T. 1988 Instability mechanisms in shear-flow transition. *Ann. Rev. Fluid Mech.* **20**, 359–391.

BERNAL, L. P. & ROSHKO, A. 1986 Streamwise vortex structures in plane mixing layers. *J. Fluid Mech.* **170**, 499–525.

BRACHET, M.-E. 1990 Géométrie des structures à petite échelle dans le vortex de Taylor–Green. *C.R. Acad. Sci. Paris* **311** (II), 775–780.

BROWAND, F. K., GUYOMAR, D. & YOON, S.-C. 1987 The behavior of a turbulent front in a stratified fluid: experiments with an oscillating grid. *J. Geophys. Res.* **92** (C5), 5329–5341.

BROWAND, F. K. & WINANT, C. D. 1973 Laboratory observations of shear-layer instability in a stratified fluid. *Boundary-Layer Met.* **5**, 67–77.

CANUTO, C., HUSSAINI, M. Y., QUARTERONI, A. & ZANG, T. A. 1988 *Spectral Methods in Fluid Dynamics*. Springer.

CAULFIELD, C. P. & PELTIER, W. R. 1994 Three-dimensionalization of the stratified mixing layer. *Phys. Fluids* **6**, 3803–3805.

COMTE, P., LESIEUR, M. & LAMBALLAIS, E. 1992 Large and small-scale stirring of vorticity and a passive scalar in a 3D temporal mixing layer. *Phys. Fluids* A **4**, 2761–2778.

CORCOS, G. M. & SHERMAN, F. S. 1976 Vorticity concentration and the dynamics of unstable free shear layers. *J. Fluid Mech.* **73**, 241–264.

CORCOS, G. M. & SHERMAN, F. S. 1984 The mixing layer: deterministic models of a turbulent flow. Part 1. Introduction and the two-dimensional flow. *J. Fluid Mech.* **139**, 29–65.

DAVIS, P. A. & PELTIER, W. R. 1979 Some characteristics of the Kelvin–Helmholtz and resonant overreflection modes of shear flow instability and of their interaction through vortex pairing. *J. Atmos. Sci.* **36**, 2394–2412.

DELISI, D. P. 1973 An experimental study of finite amplitude waves in a stratified wind tunnel. PhD thesis, University of California, Berkeley.

DRAZIN, P. G. & REID, W. H. 1981 *Hydrodynamic Stability*. Cambridge University Press.

DRITSCHEL, D. G., HAYNES, P. H., JUCKES, M. N. & SHEPHERD, T. G. 1991 The stability of a two-dimensional vorticity filament under uniform strain. *J. Fluid Mech.* **230**, 647–665.

DUTTON, J. A. & PANOFSKI, H. A. 1970 Clear air turbulence: a mystery may be unfolding. *Science* **167**, 937–944.

GARRETT, C. 1993 A stirring tale of mixing. *Nature* **364**, 670–671.

GERZ, T. & SCHUMANN, U. 1991 Direct simulations of homogeneous turbulence and gravity waves in sheared and unsheared stratified flows. In *Turbulent Shear Flow 7* (ed. F. Durst, *et al.*), pp. 27–45. Springer.

GOSSARD, E. E., RICHTER, J. H. & ATLAS, D. 1970 Internal waves in the atmosphere from high-resolution radar measurements. *J. Geophys. Res.* **75**, 3523–3535.

GREGG, M. 1987 Diapycnal mixing in the thermocline: a review. *J. Geophys. Res.* **92** (C5), 5249–5286.

HABERMAN, R. 1973 Wave-induced distortions of a slightly stratified shear layer: a nonlinear critical layer effect. *J. Fluid Mech.* **58**, 727–735.

HAURY, L. R., BRISCOE, M. G. & ORR, M. H. 1979 Tidally generated internal wave packets in Massachusetts Bay. *Nature* **278**, 312–317.

HAZEL, P. 1972 Numerical studies of the stability of inviscid stratified shear flows. *J. Fluid Mech.* **51**, 39–61.

HERRING, J. R. & METAIS, O. 1989 Numerical experiments in forced stably stratified turbulence. *J. Fluid Mech.* **202**, 97–115.

HO, C. M. & HUERRE, P. 1984 Perturbed free shear layers. *Ann. Rev. Fluid Mech.* **16**, 365–424.

HOPFINGER, E. J. 1987 Turbulence in stratified fluids: a review. *J. Geophys. Res.* **92** (C5), 5287–5303.

HOWARD, L. N. 1961 Note on a paper of John W. Miles. *J. Fluid Mech.* **10**, 509–512.

KELLY, R. E. 1967 On the stability of an inviscid shear layer which is periodic in space and time. *J. Fluid Mech.* **27**, 657–689.

KLAASSEN, G. P. & PELTIER, W. R. 1985*a* The evolution of finite amplitude Kelvin–Helmholtz billows in two spatial dimensions. *J. Atmos. Sci.* **42**, 1321–1339.

KLAASSEN, G. P. & PELTIER, W. R. 1985*a* The effect of Prandtl number on the evolution and stability of Kelvin–Helmholtz billows. *Geophys. Astrophys. Fluid Dyn.* **32**, 23–60.

KLAASSEN, G. P. & PELTIER, W. R. 1985*b* The onset of turbulence in finite-amplitude Kelvin–Helmholtz billows. *J. Fluid Mech.* **155**, 1–35.

KLAASSEN, G. P. & PELTIER, W. R. 1989 The role of transverse secondary instabilities in the evolution of free shear layers. *J. Fluid Mech.* **202**, 367–402.

KLAASSEN, G. P. & PELTIER, W. R. 1991 The influence of stratification on secondary instability in free shear layers. *J. Fluid Mech.* **227**, 71–106.

KNIO, O. M. & GHONIEM, A. F. 1992 The three-dimensional structure of periodic vorticity layers under non-symmetric conditions. *J. Fluid Mech.* **243**, 353–392.

KOOP, C. G. & BROWAND, F. K. 1979 Instability and turbulence in a stratified fluid with shear. *J. Fluid Mech.* **93**, 135–159.

KRAICHNAN, R. H. & MONTGOMERY, D. 1980 Two-dimensional turbulence. *Rep. Prog. Phys.* **43**, 547–617.

LASHERAS, J. C., CHO, J. S. & MAXWORTHY, T. 1986 On the origin and evolution of streamwise vortical structures in a plane, free shear layer. *J. Fluid Mech.* **172**, 231–238.

LAWRENCE, G. A., BROWAND, F. K. & REDEKOPP, L. G. 1991 The stability of a sheared density interface. *Phys. Fluids* A **3**, 2360–2370.

LESIEUR, M. 1990 *Turbulence in Fluids*. Kluwer.

LIENHARD, J. H. & VAN ATTA, C. W. 1990 The decay of turbulence in thermally stratified flow. *J. Fluid Mech.* **210**, 57–112.

LIN, J.-T. & PAO, Y.-H. 1979 Wakes in stratified fluids. *Ann. Rev. Fluid Mech.* **11**, 317–338.

LIN, S. J. & CORCOS, G. M. 1984 The mixing layer: deterministic models of a turbulent flow. Part 3. The effect of plain strain on the dynamics of streamwise vortices. *J. Fluid Mech.* **141**, 139–178.

LOMBARD, P. N., STRETCH, D. D. & RILEY, J. J. 1990 Energetics of a stably stratified mixing layer. *Proc. the Ninth Symp. on Turbulence and Diffusion, Roskilde, Denmark, 30 April–3 May*. Am. Met. Soc.

MASLOWE, S. A. 1972 The generation of clear air turbulence by nonlinear waves. *Stud. Appl. Maths* **51**, 1–16.

MASLOWE, S. A. 1986 Critical layers in shear flows. *Ann. Rev. Fluid Mech.* **18**, 405–432.

METCALFE, R. W., ORSZAG, S. A., BRACHET, M., MENON, S. & RILEY, J. J. 1987 Secondary instability of a temporally growing mixing layer. *J. Fluid Mech.* **184**, 207–243.

MILES, J. W. 1961 On the stability of heterogeneous shear flows. *J. Fluid Mech.* **10**, 496–508.

NYGAARD, K. J. & GLEZER, A. 1991 Evolution of streamwise vortices and the generation of small-scale motion in a plane mixing layer. *J. Fluid Mech.* **231**, 257–301.

ORSZAG, S. A. 1971 Numerical simulation of incompressible flows within simple boundaries. I. Galerkin (spectral) representation. *Stud. Appl. Maths* **50**, 293–327.

PATNAIK, P. C., SHERMAN, F. S. & CORCS, G. M. 1976 A numerical simulation of Kelvin–Helmholtz waves of finite amplitude. *J. Fluid Mech.* **73**, 215–240.

PELTIER, W. R., HALLÉ, J. & CLARK, T. L. 1978 The evolution of finite amplitude Kelvin–Helmholtz billows. *Geophys. Astrophys. Fluid Dyn.* **10**, 53–87.

PUMIR, A. & SIGGIA, E. D. 1992 Development of singular solutions to the axisymmetric Euler equations. *Phys. Fluids* A **4**, 1472–1491.

ROGERS, M. M. & MOSER, R. D. 1992 The three-dimensional evolution of a plane mixing layer: The Kelvin–Helmholtz rollup. *J. Fluid Mech.* **243**, 183–226.

SCHOWALTER, D. G., VAN ATTA, C. W. & LASHERAS, J. C. 1994 Baroclinic generation of streamwise vorticity in a stratified shear layer. *Meccanica* (Special Issue on Vortex Dynamics, ed. E. J. Hopfinger & P. Orlandi), **20** (4), 361–372.

SCOTTI, R. S. & GORCOS, G. M. 1972 An experiment on the stability of small disturbances in a stratified shear layer. *J. Fluid Mech.* **52**, 499–528.

STAQUET, C. 1991 Influence of a shear on a stably-stratified flow. In *Organized Structures and Turbulence in Fluid Mechanics* (ed. O. Métais & M. Lesieur), pp. 469–487. Kluwer.

STAQUET, C. 1994 A numerical study of vorticity layers in a two-dimensional stratified shear flow. *Meccanica* (Special Issue on Vortex Dynamics, ed. E. J. Hopfinger & P. Orlandi), **20** (4), 489–506.

STAQUET, C. & RILEY, J. J. 1989 A numerical study of a stably-stratified mixing layer. In *Turbulent Shear Flows 6* (ed. J.-C. André *et al.*), pp. 381–397. Springer.

STUART, J. T. 1967 On finite amplitude oscillations in laminar mixing layers. *J. Fluid Mech.* **29**, 417–440.

THORPE, S. A. 1968 A method of producing a shear flow in a stratified fluid. *J. Fluid Mech.* **32**, 693–704.

THORPE, S. A. 1971 Experiments on the instability of stratified shear flows: miscible fluids. *J. Fluid Mech.* **46**, 299–319.

THORPE, S. A. 1973 Experiments on instability and turbulence in a stratified shear flow. *J. Fluid Mech.* **61**, 731–751.

THORPE, S. A. 1985 Laboratory observations of secondary structures in Kelvin–Helmholtz billows and consequences for ocean mixing. *Geophys. Astrophys. Fluid Dyn.* **34**, 175–199.

THORPE, S. A. 1987 Transitional phenomena on turbulence in stratified fluids. *J. Geophys. Res.* **92** (C5), 5231–5248.

TROITSKAYA, Y. I. 1991 The viscous diffusion nonlinear critical layer in a stratified shear flow. *J. Fluid Mech.* **233**, 25–48.

WINANT, C. D. & BROWAND, F. K. 1974 Vortex pairing: the mechanism of turbulent mixing layer growth at moderate Reynolds number. *J. Fluid Mech.* **63**, 237–255.

WOODS, J. D. 1969 On Richardson's number as a criterion for laminar-turbulent-laminar transition in the ocean and atmosphere. *Radio Sci.* **4**, 1289–1298.

YOSHIDA, S. 1977 On a mechanism for breaking of interfacial waves. *Coastal Engng Japan* **20**, 7–15.

YOSHIDA, S., CAULFIELD, C. P. & PELTIER, W. R. 1994 Secondary instability and three-dimensionalization in a laboratory accelerating shear layer with varying density differences. *Preprints of 4th Intl Symp. on Stratified Flows, Grenoble, June 28–July 2* (ed. E. J. Hopfinger, B. Voisin & G. Chavand).